Nucleolar dynamics are determined by the ordered assembly of the ribosome

Jessica Sheu-Gruttadauria[1,2,†], Xiaowei Yan[1,3], Nico Stuurman[1,4], Stephen N. Floor[2,5,†], Ronald D. Vale[1,6,†]

[1] Department of Cellular and Molecular Pharmacology, University of California, San Francisco, San Francisco, CA, USA.
[2] Department of Cell and Tissue Biology, University of California, San Francisco, CA, USA
[3] Present address: Department of Dermatology, Stanford, CA, USA.
[4] Present address: Altos Labs, Redwood City, CA, USA.
[5] Helen Diller Family Comprehensive Cancer Center, University of California, San Francisco, CA, USA.
[6] Janelia Research Campus, Howard Hughes Medical Institute, Ashburn, VA, USA.

[†] Address correspondence to: JS-G jsheugrutt@gmail.com, SNF stephen@floorlab.org, RDV valer@hhmi.org

Abstract

Ribosome biogenesis is coordinated within the nucleolus, a biomolecular condensate that exhibits dynamic material properties that are thought to be important for nucleolar function. However, the relationship between ribosome assembly and nucleolar dynamics is not clear. Here, we screened 364 genes involved in ribosome biogenesis and RNA metabolism for their impact on dynamics of the nucleolus, as measured by automated, high-throughput fluorescence recovery after photobleaching (FRAP) of the nucleolar scaffold protein NPM1. This screen revealed that gene knockdowns that caused accumulation of early rRNA intermediates were associated with nucleolar rigidification, while accumulation of late intermediates led to increased fluidity. These shifts in dynamics were accompanied by distinct changes in nucleolar morphology. We also found that genes involved in mRNA processing impact nucleolar dynamics, revealing connections between ribosome biogenesis and other RNA processing pathways. Together, this work defines mechanistic ties between ribosome assembly and the biophysical features of the nucleolus, while establishing a toolbox for understanding how molecular dynamics impact function across other biomolecular condensates.

Introduction

Ribosome biogenesis, an essential process for cellular viability, growth, and proliferation[1–3], requires the coordinated activity of hundreds of assembly factors and ribosomal proteins[4,5]. These events are mainly orchestrated within the nucleolus, the most prominent biomolecular condensate in the nucleus. The nucleolus forms around rDNA loci, which encode the 47S pre-ribosomal RNA (rRNA) that is co-transcriptionally processed to yield the small subunit (SSU) associated 18S rRNA and large subunit (LSU) 28S and 5.8S rRNAs. It is comprised of three concentric subcompartments: the fibrillar center (FC), dense fibrillar component (DFC), and the granular component (GC). Each of these compartments is associated with sequential steps in ribosome assembly, beginning with rRNA transcription by RNA Polymerase I (Pol I) in the FC, followed by processing and modification in the DFC, and culminating in the GC with the assembly of the pre-SSU and LSU[6–8]. Importantly, nucleolar structure requires the steady flux of ribosome assembly, as inhibition of Pol I activity leads to disassembly of this concentric architecture[9].

Increasing evidence suggests that the nucleolus forms through biological phase transitions, driven by heterotypic, multivalent interaction networks formed between nucleolar scaffolding proteins, RNA, and intrinsically disordered regions (IDRs) in nucleolar constituents[10]. Many of these interactions are thought to occur with the developing pre-ribosome itself, which is composed of a central rRNA scaffold that recruits ribosomal proteins (RPs) and assembly factors that are rich in IDRs[11]. It has therefore been hypothesized that pre-ribosomes are retained in the nucleolus through trans interactions with scaffolding proteins[11,12], which suggests that ribosomal maturation is intimately tied to nucleolar assembly principles. However, most understanding of nucleolar formation comes from in vitro reconstitution of a subset of nucleolar constituents, making it challenging to determine how the biophysical assembly features of the nucleolus relate to its molecular function in ribosome biogenesis.

Assembly through phase separation gives rise to distinctive material properties. The nucleolus is often described as liquid-like[13,14], and it has been hypothesized that these material properties are essential for nucleolar function. For example, the concentric architecture of the nucleolus is thought to arise from the differing viscosities of each subcompartment[13]. Moreover, optogenetic clustering of nucleolar scaffolds increases nucleolar rigidity and leads to inhibition of rRNA processing[15]. Lastly, disruption of certain ribosome biogenesis steps leads to aberrant nucleolar morphologies[16–18]. However, the mechanisms that determine dynamics in the nucleolus remain poorly defined. This gap arises in large part from limited tools for characterizing the dynamics of biomolecular condensates in living systems.

Here, we introduce a platform to systematically measure macromolecular dynamics in biomolecular condensates in live cells using automated high-content fluorescence recovery after photobleaching (FRAP). We apply this strategy to screen for factors that influence the dynamics of a key nucleolar scaffolding protein, nucleophosmin (NPM1). When combined with analysis of nucleolar morphology, we identify four biophysical states of the nucleolus that are associated with specific stages in ribosome assembly. In addition, we discover a fifth biophysical state that results from disruption of diverse mRNA processing pathways. Characterizing ribosome

biogenesis in each of these biophysical states reveals that they arise from changes in the pre-ribosome composition within the nucleolus. Accumulation of early rRNA intermediates is associated with decreases in NPM1 dynamics, while accumulation of late intermediates leads to increased NPM1 exchange. These trends correlate directly with the partitioning of NPM1 into the nucleolus, which suggests that dynamics are determined by the valency of interactions between pre-ribosome intermediates and nucleolar scaffolds. We further demonstrate that mutation of key interfaces in NPM1 that mediate trans interactions with ribosomal precursors impacts both its partitioning into the nucleolar condensate as well as its macromolecular diffusivity. Together, these results support a model where the ratios of ribosomal precursors determine the dynamic properties of the nucleolus, providing a direct tie between assembly of ribosomes and the material properties of the nucleolus.

Results

HiT-FRAP: A platform for performing scalable automated FRAP

To identify factors that guide macromolecular dynamics in biomolecular condensates, we developed a platform to perform scalable, fully automated FRAP experiments (Fig. 1A), which we call HiT-FRAP. This pipeline uses data-adaptive imaging strategies to identify and bleach fluorescently-labeled organelles in living cells and acquire images to measure fluorescence recovery (Fig. 1B). By iterating bleaching and recovery over multiple fields of view, we were able to perform 50-100 bleaches per minute, which is at least two orders of magnitude higher throughput than manual approaches. We can then repeat this method across multiple wells in an arrayed format, allowing us to determine how dynamics are influenced by diverse perturbations. We also developed an analysis pipeline that quantifies intensity at bleach locations over the time course, fits recovery curves to a FRAP model, and exports parameters that describe dynamics (mobile fraction and $t_{1/2}$, which represent the percentage of mobile molecules and the time to 50% recovery, respectively) for all acquired positions. Although the HiT-FRAP pipeline can calculate parameters using multiple FRAP models (see Methods), for the present study, we fit data to a simple exponential to prevent over-fitting and find that it sufficiently describes recovery profiles for NPM1 (Fig. S1A). In addition, the HiT-FRAP analysis pipeline calculates multiple morphological parameters that describe size, shape, and intensity features from segmented images (see Methods).

We then applied HiT-FRAP to monitor dynamics in the nucleolus, focusing on the GC scaffolding protein NPM1, which is thought to contribute directly to nucleolar phase separation[10]. We appended mNeonGreen or mScarlet to the C-terminus of endogenous NPM1 in HeLa cells to avoid potential artifacts associated with ectopic overexpression. Both tagging strategies show similar localization patterns and FRAP recoveries (Fig. S1B) that are in keeping with published values[19] ($t_{1/2}$ ~2 seconds, Fig. 1C and S1B). In addition, we applied HiT-FRAP to measure relative differences in NPM1 dynamics and nucleolar morphology upon perturbation. It has been previously demonstrated that depletion of ATP results in a decrease in NPM1 mobility and an increase in morphological irregularity[13,20]. Therefore, we rapidly depleted ATP with 2-deoxyglucose (2-DG) and sodium azide for ten minutes to block both glycolysis and oxidative

phosphorylation. As previously observed, we found that NPM1 exhibited slower recovery (~1.5-fold) and a lower percentage of mobile molecules (~2-fold) as compared to vehicle alone (Fig. 1C). Morphological analysis also captured a decrease in circularity of about 15% (Fig. 1 C and D), further validating the pipeline. These results demonstrate that HiT-FRAP enables automated FRAP measurements and analysis that can robustly quantify changes in nucleolar dynamics and morphology upon perturbation.

Systematic identification of factors that impact nucleolar dynamics

We then applied HiT-FRAP to systematically identify factors that impact NPM1 dynamics in the nucleolus. We chose to focus initially on RNA helicases, which have been proposed to act as global regulators of cellular phase separation by modulating RNA interactions that underlie the formation of many cellular condensates[21,22]. Indeed, it has been hypothesized that the chaperoning activity of RNA helicases may be responsible for broadly maintaining condensate dynamics and preventing aggregation[21,23]. Many RNA helicases also localize to the nucleolus, where they are thought to coordinate multiple steps in ribosome biogenesis[24]. Therefore, we depleted 65 RNA helicases alongside 9 pairs of phylogenetically related helicases that may act redundantly using an arrayed siRNA library (Fig. S2A) and monitored NPM1 dynamics using HiT-FRAP. This screen identified 13 RNA helicases or helicase pairs whose depletion significantly impacted $t_{1/2}$ and 9 helicases or pairs that showed significant changes in mobile fraction (Fig. 2A and Fig. S2B), totaling 15 unique helicases or helicase pairs that impact NPM1 dynamics. We replicated these hits in the mScarlet cell line (Fig. S2C), validated the gene depletion strategy using depooled guide RNAs (Fig. S2D), and assessed knockdown by western blot for select significant hits (Fig. S2E). Notably, we observed a modest indirect correlation ($r = -0.67$, p-value = 0.01) between $t_{1/2}$ and mobile fraction for hits (Fig. S2F), where those that exhibit faster recovery also show a significant increase in the percentage of mobile molecules. This correlation suggests that the disruptions in nucleolar dynamics we observe alter both the kinetic determinants of exchange and the population of molecules that can move within the nucleolar condensate. Given this relationship, we chose to focus further analysis on those factors that impact kinetics.

Either the human or yeast homologs of 8 out of the 13 helicases that influence $t_{1/2}$ localize to the nucleolus or are implicated in ribosome biogenesis (Fig. 2A). Of these helicases, those that led to faster recovery (DDX18[25], DDX54[26], DDX55[27]) are mainly involved in LSU assembly, where they directly interact with rRNA and likely catalyze remodeling necessary for ribosomal maturation. Conversely, 3 out of 4 nucleolar helicases that led to slower exchange are thought to coordinate early rRNA processing via the SSU processome (DDX41[28], eIF4A3[29] and IGHMBP2[30]). The notable exception was co-depletion of DDX5 and DDX17, which remodels the LSU 28S rRNA[31]. However, all of these “slow” hits also participate in other RNA processing pathways, including pre-mRNA processing, nonsense mediated decay (NMD), and translation[32], which could contribute to the phenotype we observe. Moreover, the remaining non-ribosome biogenesis-associated helicases that we identified also led to slower dynamics and participate in similar RNA processing pathways (AQR, DHX8, DHX38, eIF4A1+eIF4A2, and UPF1).

To better understand how these helicases are leading to nucleolar disruption, we designed a secondary screen comprised of 290 additional gene depletions (Fig. 2B). 51% of the secondary library targeted ribosome biogenesis factors, including every ribosomal protein and select assembly factors involved in transcription, SSU, and LSU assembly. The remainder of the library was composed of STRING-database[33] interactors for the helicase hits, targeting multiple RNA processing pathways including pre-mRNA splicing, transport, translation, and degradation. From this secondary screen, we identified 55 "slow" and 21 "fast" hits that led to significant increases and decreases in $t_{1/2}$, respectively (Fig. 2C). We observed a similar correlation between mobile fraction and $t_{1/2}$ as seen in our primary screen (Fig. S2G). Functional analysis showed that fast hits were enriched for LSU-associated assembly factors and ribosomal proteins (Fig. 2D), indicating that the original RNA helicase hits DDX18, DDX54, and DDX55 might impact NPM1 dynamics through broad disruption of LSU maturation. Conversely, slow hits were enriched for pathways outside of ribosome biogenesis, including mRNA splicing, processing, and NMD (Fig. 2D). These results suggest that depletion of DDX5+DDX17, DDX41, eIF4A3, and IGHMBP2 may impact nucleolar dynamics through their non-ribosome biogenesis roles, likely downstream of pathway inhibition. Taken together, we conclude that the RNA helicases we identify are impacting NPM1 dynamics through disruption of their specific biochemical activities in ribosome biogenesis or mRNA processing pathways.

Phenotypic clustering of NPM1 dynamics and morphological features couples nucleolar biophysical state to co-functional gene groups

Further image analysis revealed that perturbations impacting NPM1 dynamics also exhibited striking changes in nucleolar morphology (Fig. 2A and C). Therefore, we sought to describe the biophysical state of the nucleolus by expanding our analysis to include six nucleolar feature parameters: $t_{1/2}$, mobile fraction, circularity, eccentricity, mean intensity, and area (Fig. 3A). To minimize false positives, we calculated a phenotype score for each of these features across both the primary RNA helicase and secondary interactor screens that incorporated both the statistical significance and effect size between gene-depleted versus a subset of control (NT) samples (see Methods), which we visualized by performing dimensionality reduction through principal component analysis (PCA, Fig. 3A and B, Fig. S3A). Hits were grouped by separation from the NT cluster and similarity in PCA space in at least two out of three biological replicates (Fig. S3B). We also replicated the screen and our analysis with the mScarlet cell line and found that both results were largely in agreement, which supports that most effects we observe do not result from tagging artifacts (Fig. S3C).

We then categorized these hits by their biological function. Interestingly, genes that share related functions tended to reside in proximal regions within phenotypic PCA space (Fig. S3D). We therefore performed hierarchical clustering using phenotypic z-scores, which identified five unique nucleolar biophysical states (Fig. 3C and D). Four out of five of these states were associated with genes involved in ribosome biogenesis. Detailed examination of these gene clusters revealed enrichment for factors that mediate specific steps in ribosome assembly, allowing us to define nucleolar biophysical signatures associated with early processing stages (Fig. 3D, "Early"), the RNA exosome, which is responsible for rRNA end-processing throughout

biogenesis (Fig. 3D, “RNA Exosome”), and two groups involved in LSU assembly (Fig. 3D, “LSU1” and “LSU2”). The fifth cluster, conversely, was comprised of factors with no known role in ribosome biogenesis (Fig. 3D, “Other”) and included most of the “slow” hits identified by HiT-FRAP. These results suggest that nucleolar assembly features are tightly related to key steps in its core function of ribosome biogenesis. Moreover, despite the diversity of their associated pathways, most non-ribosome biogenesis-associated hits corresponded with the same nucleolar biophysical state, which suggests these factors may be impacting assembly features of the nucleolus through a shared mechanism.

Inhibition of rRNA transcription or the RNA exosome leads to nucleolar fragmentation

We identified a small phenotypic cluster enriched for factors involved in very early stages of ribosome assembly, including PolR1a, the largest component of the RNA Pol I complex, and components of the UTPA complex (HEATR1, UTP15, and WDR43) that functions within the 5′ETS particle and SSU processome (Fig. 3C and D). Morphologically, depletion of these genes led to nucleolar fragmentation and rounding (Fig. 3D). In addition, loss of these factors decreased NPM1 dynamics, which aligns with recent reports that Pol I inhibition leads to slowed NPM1 exchange[34]. However, we note that the size of the nucleolus in this cluster approaches the size of the bleach point, and therefore, we are reporting primarily on exchange with the nucleoplasm as opposed to internal rearrangements, confounding direct comparison with other hits in the screen.

These early assembly factors share roles in positively regulating rRNA transcription, which suggests that ablation of Pol I activity may lead to the phenotype we observe. In support of this idea, nucleolar fragmentation and rounding upon Pol I inhibition has been widely reported in the literature[9]. We tested this hypothesis by treating cells with low doses (0.04 μg/mL) of Actinomycin D (ActD)[35,36] and 500 nM CX5461[37], which are selective Pol I inhibitors. We found that acute treatment (2 hours) with ActD or CX5461 fully recapitulated the Early phenotypic cluster (Fig. 4A, Fig. S4A), confirming that loss of rRNA transcription drives this nucleolar phenotype.

Given that NPM1 condensation is thought to be driven by interactions with assembling ribosomes, we hypothesized that nucleolar fragmentation may result from the loss of rRNA intermediates in the nucleolus. Therefore, we quantified levels of nucleolar rRNA precursors with RNA FISH using probes against pre-rRNA interspacer regions: the 5′ETS, ITS1, and ITS2, which are processed in early/SSU, SSU, and LSU-associated maturation stages, respectively. We find that after 2 hours of exposure to low-dose ActD, all rRNA precursors were depleted from the nucleolus, which supports the role of pre-ribosome intermediates in maintaining nucleolar structure (Fig. 4B).

We also found that a cluster containing core components of the RNA exosome resulted in nucleolar fragmentation (Fig. 3C), but unlike the Pol I-associated cluster, exhibited a more irregular nucleolar shape and decrease in NPM1 intensity (Fig. 3D). In ribosome biogenesis, the RNA exosome coordinates 3′-5′ trimming of the 5′ETS, ITS1, and ITS2. The substrates of this and other functions of the RNA exosome are specified by adaptor proteins[38], many of which we

targeted in the screen (NOP53, UTP18, WDR3, NOP58, PAPD7, PDCD11, RMB7, ZCCHC7, and ZCCHC8). Depletion of RNA exosome adaptors that function outside of ribosome biogenesis did not lead to a nucleolar phenotype. Conversely, NOP53, which directs the exosome to process the ITS2 in LSU maturation[39], resided within the LSU-associated phenotypic cluster apart from other exosome components (Fig. 3C and D). Within the RNA exosome cluster, however, we identified key components of the 5′ETS particle, including UTPB (DDX21, PWP2, WDR3, WDR36) and Sof1-UTP7 (WDR46) components, which in yeast has been shown to recruit the exosome for 5′ETS processing early in ribosome biogenesis[39] and suggests that the observed phenotype may arise from disruption of these early processing events. Importantly, these early processing steps are coupled with rRNA transcription[40]. Therefore, we hypothesized that the fragmentation we observe for the RNA exosome phenotypic group may result from depletion of rRNA intermediates in the nucleolus as seen in the Early/Pol I cluster. Consistent with this idea, we found that knockdown of the core RNA helicase of the exosome, SKIV2L2, led to a modest but significant depletion of all precursors from the nucleolus (Fig. 4B). Notably, this depletion was far less substantial than seen with inhibition of Pol I, which could explain the differences we observe in organelle shape. Together, these results indicate that fragmentation of the nucleolus results from depletion of nucleolar ribosome intermediates.

Disruption of key stages in late LSU maturation leads to distinct nucleolar phenotypes

We identified two clusters of LSU-associated RPs and assembly factors (LSU1 and 2), in keeping with the GC's central role in LSU maturation and previous reports of nucleolar disruption upon depletion of LSU RPs[18]. These clusters exhibited similar but distinguishable phenotypes, with LSU1 exhibiting a strong increase in nucleolar size, and LSU2 showing a more irregular shape and a substantial decrease in intensity and $t_{1/2}$ (Fig. 3C and D). Recently, structural efforts have demonstrated that LSU maturation proceeds through at least eight nucleolar intermediates, States A-H[41]. Mapping the LSU clusters onto these structures revealed that LSU1 was primarily enriched for factors involved in earlier stages of LSU assembly (States A-F), while LSU2 contained factors that associate with later intermediate species (States G and H), most notably all components of the 5S RNP, a core component of the central protuberance (CP) that is thought to bridge LSU functional centers[42,43] and mediate intersubunit communication with the SSU[44] (Fig. 4C).

To determine whether these differences in nucleolar phenotypes arise from distinct changes in ribosome biogenesis, we assessed rRNA intermediate composition in the nucleolus by FISH for strong hits in both the LSU1 and LSU2 clusters (LSU1: NSA2; LSU2: RPF2). We observed a significant nucleolar depletion of the 5′ETS and ITS1 for both groups, as well as an accumulation of ITS2 (Fig. 4D). On a global level, however, we saw reduction of all rRNA processing intermediates and loss of the mature 28S (Fig. S4C). As ITS2 is processed after nucleolar export in the nucleoplasm, this result suggests that the phenotypes we observe result from depletion of early pre-ribosome intermediates and an accumulation of aberrant LSU precursors in the nucleolus, leading to a global defect in LSU biogenesis.

We therefore hypothesized that the distinct phenotypes we observe for LSU1 and LSU2 may result from the buildup of different LSU precursors. Indeed, the difference between factors in the LSU1 and LSU2 clusters implicates the transition from State F to G, which involves removal of a protein interaction network that allows for binding of factors critical for downstream maturation[41,45]. The State F to G transition is irreversible and mediated by the AAA+ ATPase MDN1[41,46] (Fig. 4C). To test whether the differences between the LSU1 and LSU2 clusters arise from the inability to remove the State F protein interaction network, we depleted MDN1. We found that MDN1 depletion fully recapitulated the LSU1 phenotype (Fig. 4E, Fig. S4D), which suggests that the LSU1 and LSU2 clusters are distinguished by the MDN1-mediated removal of the protein interaction network that licenses transition from State F to G.

We then sought to further characterize the LSU precursors that accumulate in the LSU1 and LSU2 clusters using immunofluorescence to measure nucleolar colocalization of intermediates both up and downstream of the F-G transition (Fig. 4C). To identify intermediates upstream of State G, we monitored localization of NOP2, a protein removed by MDN1. The NOP2 protein interaction network shares a mutually exclusive binding site with NOG2 and NOP53, which we used as markers for States G and H. When we depleted the LSU1 gene NSA2, we found a strong enrichment for NOP2 (Fig. 4F), which suggests that states upstream of G and H accumulate in the LSU1 phenotypic cluster. We observed a similar accumulation upon depletion of MDN1 (Fig. S4E), as seen previously upon knockdown of the yeast MDN1 ortholog, Rea1[45]. Interestingly, we also observed a modest increase in nucleolar NOG2 upon depletion of both NSA2 and MDN1 (Fig. 4F and S4E). Therefore, it is possible that some of these upstream intermediates can still recruit downstream markers, likely forming aberrant complexes that remain sequestered in the nucleolus. The accumulation of multiple intermediates may explain the increase in nucleolar size we see in this phenotypic cluster (Fig. 3D). Alternatively, these factors may be recruited in preparation for association and represent an unbound, latent population.

Conversely, when we depleted the LSU2 factor RPF2, we observed a strong depletion of NOP2 from the nucleolus and enrichment for State G and H markers (Fig. 4F). We confirmed this effect for another LSU2 cluster factor, NOG2 (Fig. S4E). These results suggest that when LSU2 assembly factors are depleted, maturation can proceed through the critical F to G transition, but then stalls with the formation of partially assembled State G and H intermediates that accumulate within the nucleolus. Moreover, these results imply that critical structural changes must occur during State G/H maturation to license nucleolar export. Given that all 5S RNP factors fall in the LSU2 group and previous hypotheses in the field[18], this transition likely surrounds 5S RNP rotation and stable formation of the mature CP, serving as a quality control step governing export.

Perturbation of diverse mRNA processing pathways results in slowed NPM1 dynamics and accumulation of rRNA precursors in the nucleolus

The last phenotypic cluster was primarily composed of factors with no known direct role in ribosome assembly (Fig. 3D, “Other”). Phenotypically, this gene group showed reduced

dynamics, increases in circularity, and modest decreases in size (Fig. 3D). This cluster was enriched for genes that coordinate diverse mRNA processing pathways, including NMD, the exon junction complex (EJC), and pre-mRNA splicing, particularly members of the SF3b spliceosome complex (Fig. 5A). We note, however, that the NMD-associated phenotype was less reproducible in the mScarlet NPM1 tagged cell line (Fig. S2C) and therefore, we chose to focus further characterization on the more robust hits.

To further validate the relationship between nucleolar assembly and pre-mRNA splicing, we treated cells with an inhibitor of the SF3b complex, pladienolide B (PladB). Notably, PladB is known to inhibit splicing in under four hours[47]. We found that nucleolar rounding begins on a similar time scale (approximately 2 hours) after treatment with 10 nM PladB (Fig. 5B and S5A), which suggests direct crosstalk between splicing factors and nucleolar morphology. We did not, however, observe a reduction in dynamics at these time points. Conversely, extended incubation with PladB (24 hours) robustly phenocopied genetic ablation of pre-mRNA splicing factors (Fig. 5B and S5A), validating our screen results and suggesting that the impact on dynamics we observe results from accumulated disruption of spliceosome-mediated processes.

Given the finding that nucleolar disruption is associated with discrete changes in ribosome biogenesis, we hypothesized that depletion pre-mRNA processing genes may lead to a defect in nucleolar ribosome assembly. Therefore, we performed rRNA FISH for cells depleted of PHF5A, a core component of the SF3b spliceosome complex and a robust hit in the novel gene phenotypic cluster. To determine whether disruption of the non-splicing genes we identified showed similar impacts on rRNA processing status, we also depleted CNOT1, the central scaffold for the CCR4-NOT deadenlyase complex whose nuclear roles include mRNA export and RNA surveillance. For both genes, we found nucleolar enrichment for ITS1 and 2, and for PHF5A, the 5′ETS (Fig. 5C). This enrichment did not correspond to a global increase in mature rRNAs, however, which we assessed using qPCR (Fig. S5B). Therefore, these results suggest that depletion of this novel gene group leads to an accumulation of aberrant, early precursors in the nucleolus, resulting in an overall decrease in ribosome biogenesis. Moreover, these findings support that disruption of nucleolar form can be predictive of defects in ribosome assembly.

Changes in NPM1 dynamics are associated with shifts in ribosome intermediate balance in the nucleolus

It is thought that phase separation of NPM1 is driven through direct interactions with pre-ribosome intermediates, mediated by heterotypic, multivalent interactions with rRNA and, to a lesser extent, arginine-rich (R-rich) intrinsically disordered regions[10,12,48]. Bioinformatic analysis of published ribosome intermediate structures from *S. cerevisiae* has also shown that the valency of these heterotypic interaction interfaces decrease as the ribosome matures through release of assembly factors and folding of rRNA[49]. These findings have led to a model where progressive decrease in the effective valency of interactions with nucleolar scaffolds such as NPM1 thermodynamically drives the forward assembly of the ribosome and, ultimately, release into the nucleoplasm .

Based upon our analysis of ribosome biogenesis intermediates in the nucleolus across the phenotypic clusters we identified, we found that the balance of nucleolar pre-ribosome intermediates was strongly correlated with impact on NPM1 dynamics. Accumulation of early rRNA intermediates in the novel gene group was associated with slower exchange, while depletion of early intermediates and accumulation of very late LSU precursors (States G and H, associated with the LSU2 gene group) accompanied faster exchange. At the extreme, depletion of all nucleolar rRNA precursors upon RNA Pol I inhibition and perturbation of the RNA exosome led to nucleolar fragmentation. This trend suggests that the buildup of strongly interacting, early ribosomal precursors with high valency limits NPM1 mobility, while accumulation of low valency, late pre-ribosome intermediates allow NPM1 to exchange more readily. Indeed, the transition from State F to G/H, which differentiates LSU1 and LSU2, involves the stabilization of several 28S rRNA domains[41], which could result in a significant decrease in rRNA valency and contribute to the increase in dynamics we see for LSU2 genes. These observations are consistent with a model where the strength of interactions with NPM1 may determine not only the propensity to phase separate into the nucleolar condensate, but also macromolecular dynamics.

In support of this idea, we saw a modest direct correlation between organelle intensity and $t_{1/2}$ in the screen, suggesting that slower exchange is associated with more nucleolar NPM1 ($r = 0.53$, $p < 0.0001$, Fig. S6A). Phase separation of NPM1 into the nucleolus is represented by the partition coefficient, which is the ratio of NPM1 inside versus outside the nucleolus. Therefore, to more quantitatively explore whether phase separation of NPM1 correlates with dynamics in the screen, we calculated the partition coefficient for select hits across phenotypic clusters. We observed a strong direct correlation between partitioning behavior and $t_{1/2}$ (Fig. 6A, $r = 0.87$, $p = 0.0001$). Notably, the partition coefficient for core scaffolds is directly related to the thermodynamic stability of interactions that drive phase separation[12]. Therefore, these results support the idea that the mechanisms underlying phase separation may also determine scaffold dynamics.

NPM1 dynamics are determined by interactions that drive partitioning into the nucleolus

To experimentally interrogate how the interactions that drive phase separation may impact dynamics, we examined what was known about phase separation of NPM1 in vitro. NPM1 is a multi-domain protein consisting of an N-terminal pentamerization domain, an intrinsically disordered linker region, and a C-terminal RNA-binding three-helix bundle (Fig. 6B). While all domains are necessary for phase separation, heterotypic interactions with R-rich proteins and rRNA are best studied within the intrinsically disordered linker region[10]. In addition, in the presence of crowding agents, homotypic interactions between the IDR in different NPM1 molecules can also drive phase separation[48], although these appear to contribute less strongly to partitioning in cells[12].

We therefore chose to focus on how the IDR of NPM1 contributed to partitioning and dynamics in cells. The IDR exhibits a charged block pattern composed of two acidic, negatively charged regions that alternate with two basic, positively charged regions (Fig. 6B). The two acidic domains A2 and A3 mediate heterotypic interactions with positively charged R-rich linkers in

nucleolar proteins while B1 and B2 bind to rRNA[10]. Homotypic interactions are mediated, in turn, through interactions between A3 and B2[48]. To determine how these domains contribute to NPM1 phase separation and dynamics in cells, we generated lentiviral constructs with mScarlet-tagged NPM1 where we selectively mutated charged domains in the IDR, similar to those used previously in vitro[48,50] (Fig. 6B). We abolished the negative charge of A2 and A3 by replacing them with $(GGS)_4G$ and $(GGS)_9G$ linkers, respectively, which we call $NPM1^{mA2}$ and $NPM1^{mA3}$. For the basic regions B1 and B2, we generated $NPM1^{mB1}$ and $NPM1^{mB2}$, where we mutated all lysines to alanines apart from those within annotated nuclear localization signals.

We then introduced these constructs into unedited HeLa cells and calculated their associated partition coefficients (Fig. 6C). We found that $NPM1^{mA2}$ showed a decrease (~30%) in nucleolar partitioning, which likely results from loss of interactions with R-rich nucleolar proteins. Similarly, mutating the smaller basic tract in $NPM1^{mB1}$ resulted in a modest decrease (~20%) in partitioning behaviors. Neutralization of the larger A3 tract, however, led to a ~30% increase in partitioning into the nucleolus, while loss of B2 resulted in a ~75% decrease of nucleolar localization. The substantial increase in partitioning upon removal of A3 supports in vitro findings that suggest homotypic inter- or intramolecular binding between A3/B2 may tune the availability of each region for heterotypic interactions, potentially acting as a regulatory switching mechanism[48]. However, these results also strongly suggest that the basic B2 region contributes most substantially to nucleolar partitioning, likely through interactions with rRNA.

To understand how these partitioning behaviors impact NPM1 dynamics, we monitored the recovery of the mutant constructs using HiT-FRAP (Fig. 6D). Importantly, we found that the dynamics of these mutant constructs were directly correlated to their partitioning behaviors. The strongly partitioning construct $NPM1^{mA3}$ showed a ~20% increase in $t_{1/2}$. Conversely, $NPM1^{mA2}$ and $NPM1^{mB2}$, which partitioned more weakly, exhibited significantly faster recoveries (~20% and 40%, respectively). These findings are consistent with a model where the thermodynamic forces that drive NPM1 into the nucleolar condensate also determine its macromolecular dynamics (Fig. 6E). Furthermore, they suggest that interactions between the positively charged B2 tract and RNA may be the strongest determinant of NPM1 dynamics.

Discussion

Defining the molecular determinants of condensate dynamics is an outstanding challenge in the field. Emerging work using in vitro reconstituted phase separating systems has begun to shed light on these principles, but connecting these findings to condensates in living systems has been challenging and limits the ability to relate these features to molecular function. Here, we systematically identified factors that influence nucleolar dynamics and morphology. Our findings identify co-functional gene groups that lead to distinct nucleolar biophysical signatures associated with disruption of ribosome assembly stages. In addition, we identify novel crosstalk between mRNA processing pathways and ribosome biogenesis, where disruption of pre-mRNA splicing leads to nucleolar accumulation of misprocessed rRNA precursors. Importantly, these results connect in vitro characterization of NPM1 phase separation to its biological function in ribosome assembly and suggest that its dynamics are dependent upon the pre-ribosome

intermediates that it interacts with. Early precursors that can participate in high valency interactions lower NPM1 dynamics, while low valency late precursors enable increased dynamic exchange. These results form a physical picture where nucleolar scaffold dynamics are determined by the valency and thermodynamic strength of heterotypic interactions that drive condensate formation, as seen in other network fluids[51].

Notably, collective evidence suggests that the nucleolus is a complex fluid that exhibits non-uniform composition and material features[52]. This idea is supported functionally, as biogenesis must proceed directionally, beginning with transcription, traversing processing steps through concentric subcompartments, and ending in release at the nucleolar surface. Indeed, in situ structural studies of the nucleolus show a gradient of subunit intermediates that are more mature as they near the nucleoplasm[53]. Recently, it has also been shown that the nucleolus is a viscoelastic structure built on the radial movement of ribosomal RNA, which forms a gel-like structure that fluidizes with progressive processing as it approaches the nucleolar periphery[52]. The phenotypic clusters we identify likely represent a blockade in ribosomal assembly flow, disrupting the steady-state balance of precursors within the GC and leading to the changes in dynamics we observe. Our findings also suggest that NPM1 dynamics are more sensitive to interactions with RNA, which supports that ordered rRNA maturation is likely the key factor that determines nucleolar dynamics. Therefore, it is probable that NPM1 dynamics vary spatially within the nucleolus, potentially forming a more cross-linked gel closer to sites of transcription. Exploring this idea and how it may facilitate sequential ribosomal assembly steps will require higher-resolution methods for measuring molecular dynamics and will be an exciting area for future inquiry.

Our multiparametric analysis also allows us to connect morphological features to scaffold dynamics. Simple liquids and solids can be discriminated by shape, where liquids coalesce into round structures while solids exhibit more amorphous features. Interestingly, we see that increased NPM1 dynamics tend to accompany irregular shapes (e.g. LSU clusters), while slower exchange correlates with rounding (e.g. Other cluster). This observation may be unexpected, given the historical use of NPM1 exchange as a proxy for the liquid-like features of the nucleolus. This finding suggests that 1.) the dynamics of specific scaffolds may not correspond directly to material properties or 2.) the complex physical features of the nucleolus may not follow the laws of a simple liquid. These possibilities are supported by the discovery that nucleolar shape is dictated by elastic features that arise from entanglement of unprocessed rRNA transcripts[52]. However, we found that accumulation or depletion of early precursors, which should presumably be more entangled, correspond with circular and aspherical shapes, respectively. This finding suggests that additional factors may contribute to nucleolar morphology. Future work characterizing the spatial organization of rRNA folding and recruitment of protein binding partners as rRNA matures within the nucleolus will be necessary to understand the contributions of different components to the physical state of the nucleolus. In addition, how the dynamics of NPM1 and other nucleolar constituents relate to the material properties of the entire condensate will be an intriguing focus for future work.

In addition, our results shed additional light on mechanisms underlying nucleolar ribosome maturation. For example, the LSU-associated phenotypic signatures provide insights into molecular features that license LSU release from the nucleolus. Previous work has shown that depletion of the core ribosomal proteins of the 5S RNP uL5 and uL18 led to a similar nucleolar phenotype as the LSU2 group[18], which was thought to result from the loss of interactions between R-rich linkers in uL18 and NPM1[7,18]. However, our finding that NPM1 phase separation is more strongly impacted by interactions with rRNA as opposed to R-rich linkers suggests that additional factors may contribute to the observed phenotype. Our results also support that nucleolar release requires major architectural changes that occur with installation of the 5S RNP and formation of the CP, as previously preposed[7,11,18]. Indeed, although the exact function of the CP is still under investigation, it is thought to coordinate maturation of LSU functional centers[42,43] and mediate intersubunit bridges[44,54], making its assembly a critical quality control checkpoint. CP formation is also tied to stabilization of several rRNA elements within the 28S rRNA domain V, including the L1 stalk[41,45,55,56]. This region could provide the valency necessary for sequestration within the nucleolar condensate. Further study molecularly characterizing the aberrant, export-incompetent intermediates we have identified may uncover the structural elements responsible for licensing release.

We also discovered unexpected ties between ribosome biogenesis and diverse mRNA processing pathways, most notably pre-mRNA processing. Interestingly, 5′ETS cleavage is a stress-regulated checkpoint that stalls during acute stress, resulting in the accumulation of unprocessed rRNAs that are stored within the nucleolus to maintain its structure. Once stress is lifted, processing of these rRNAs continues[57]. This phenotype is strikingly reminiscent of the splicing-associated nucleolar signature, which suggests that it may result from a similar checkpoint. In support of this idea, disruption of splicing has been shown to induce stress granule formation and proteotoxic stress[58,59]. We therefore hypothesize that disruption of genes in the non-ribosome biogenesis-associated phenotypic cluster may induce a cellular stress response that inhibits early rRNA processing steps, resulting in the accumulation of processing intermediates that we observe. This discovery also highlights the advantage of our screening approach in connecting condensate function more broadly to other cellular pathways.

In conclusion, our work establishes that nucleolar dynamics are shaped by interactions between scaffolds and ribosome intermediates. This finding implies that these interactions may play important roles in chaperoning assembly, as has been recently suggested for the NPM1 ortholog in yeast[60]. Future work will be necessary to uncover the role of phase-separating scaffolds and their dynamic behaviors in this assembly process. Moreover, our results support a model where the same molecular interaction networks that drive phase transitions in condensates may also dictate their dynamics. Therefore, dynamics may be tunable by the network connectivity principles recently proposed to broadly underlie the formation of diverse biomolecular condensates[61]. Indeed, diseases that manipulate this network in the nucleolus have been previously shown to impact nucleolar dynamics and disrupt function[50,62–64]. This model may also shed light on driving forces for poorly dynamic, pathological inclusions of phase-separating proteins[65], which could arise from shifts in the stoichiometries of interactors. Lastly, we anticipate our observations may apply to other biomolecular condensates, as many are formed through

similar networking interactions with a core set of scaffolds. HiT-FRAP now provides a toolset for uncovering the principles that drive dynamics across other biomolecular condensates and, importantly, lays the groundwork for connecting these principles to condensate function in the cell.

Author contributions

Conceptualization, J.S-G. with input from R.D.V.; Investigation, J.S-G.; Writing – Original Draft, J.S-G.; Writing – Review & Editing, J.S-G., S.N.F., R.D.V. with input from X.Y. and N.S.; Methodology, J.S-G., X.Y., N.S.; Resources, J.S-G. and R.D.V.; Formal analysis, J.S-G., X.Y., N.S.; Software, J.S-G., X.Y., N.S.; Funding Acquisition, J.S-G., S.N.F., and R.D.V.; Supervision, S.N.F. and R.D.V.

Acknowledgments,

We thank members of the Floor and Vale labs for feedback on this work and their continued support. JS-G is a Hanna H. Gray Fellow of the Howard Hughes Medical Institute. This work was supported by the National Institutes of Health R35GM149255 (to SNF). SNF is a Pew Scholar in the Biomedical Sciences, supported by The Pew Charitable Trusts. RDV is supported by the Howard Hughes Medical Institute.

Competing interests

None declared.

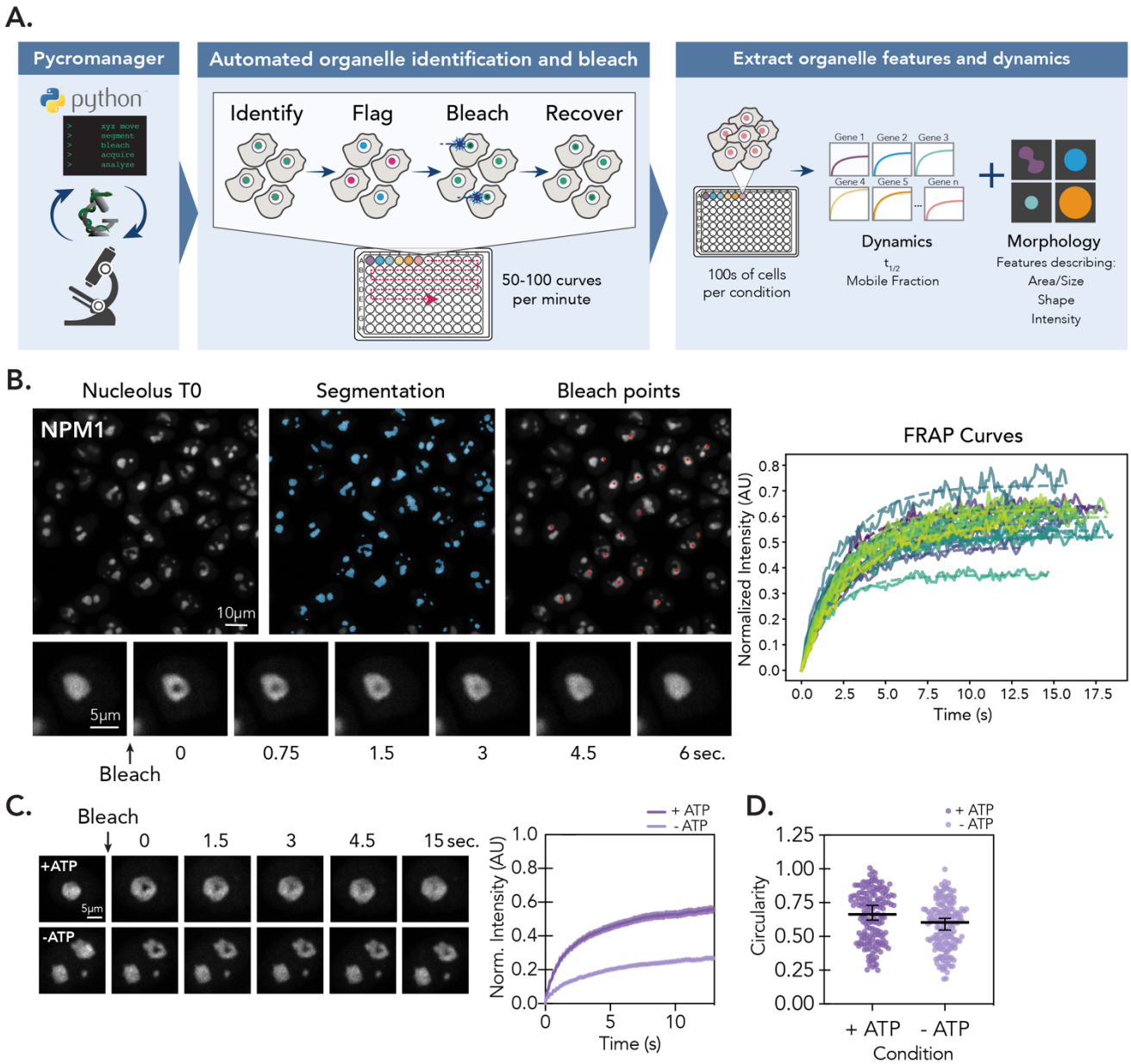

Figure 1: HiT-FRAP: A platform for performing scalable, automated FRAP experiments. (A) Schematic overview of HiT-FRAP pipeline. See also: Methods. (B) Example images show automated FRAP steps. Left, segmentation of fluorescently-labeled nucleoli (blue masks, see methods) and bleach point determination (red points). Below, zoom of single nucleolus bleach and recovery time course. Right, normalized FRAP curves generated from a single field of view. Raw intensities shown as solid line, single-exponential curve fit shown as dotted line. (C) NPM1-mNeonGreen cell lines were treated with 10 mM sodium azide and 6 mM 2-deoxyglucose for 10 min. to deplete cellular ATP prior to bleaching experiment. Left, images of single nucleolus bleach and recovery time course for vehicle and ATP deplete. Right, FRAP curves (n = 250 nucleoli, error bars are 95% CI). (D) Circularity measurements for vehicle and ATP deplete nucleoli. (n = 500 nucleoli, mean ± SD shown).

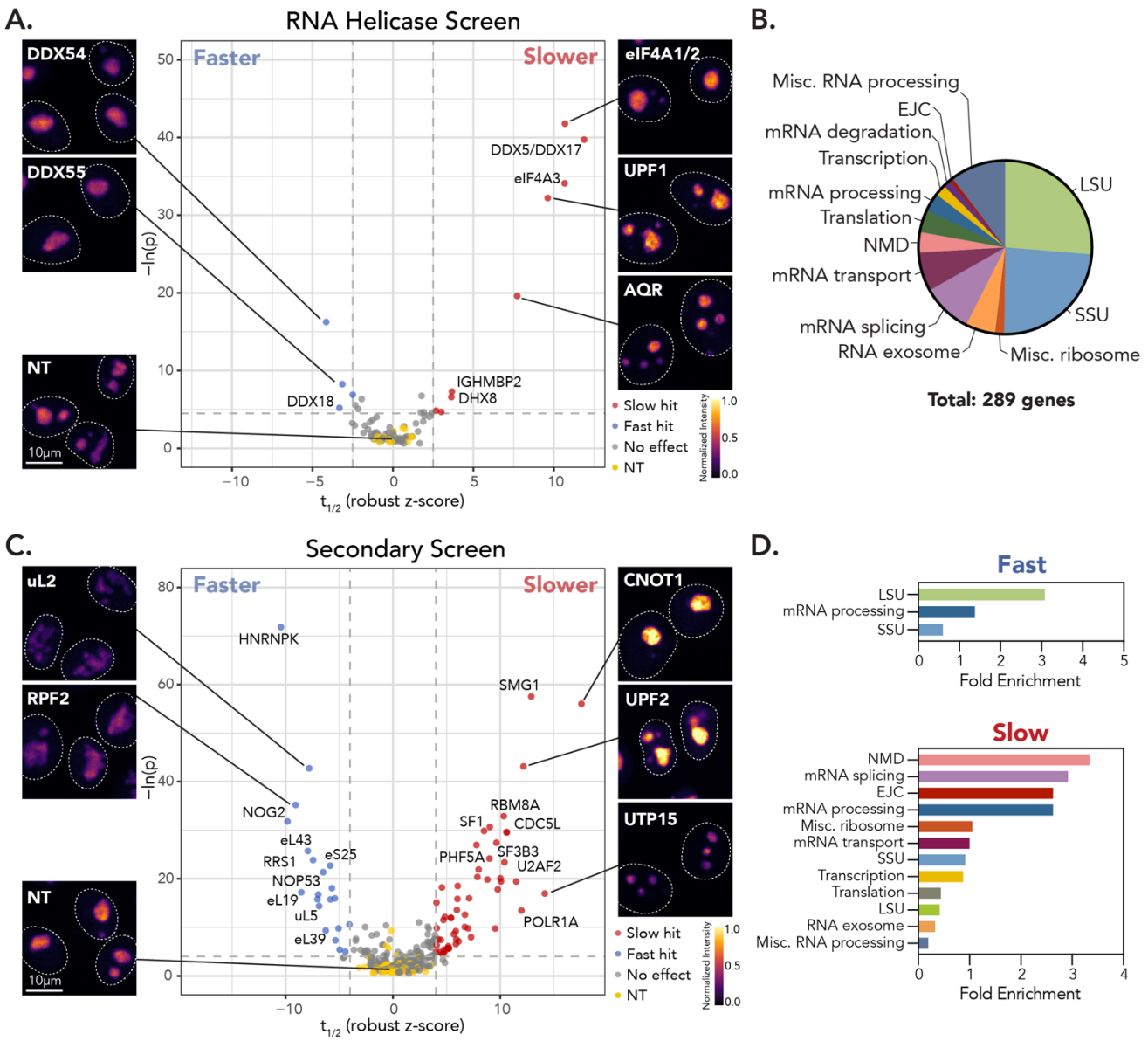

Figure 2: HiT-FRAP identifies RNA helicases and RNA processing factors that impact nucleolar dynamics. (A) Selected images and volcano plot for $t_{1/2}$ for primary RNA helicase screen, highlighting helicase hits that resulted in increased (red, "slower") or decreased (blue, "faster") $t_{1/2}$ relative to non-targeting control cells (yellow; FDR < 0.05 and z-cutoff of ± 2.5 shown as dotted lines, see Methods). Non-significant gene targets shown in gray. x-axis plots robust z-score for $t_{1/2}$ (see Methods). Images are scaled equally and colored linearly with mp-inferno LUT. (B) Functional gene distribution of secondary screen by manual annotation. (C) Selected images and volcano plot as in (A) for secondary screen. (FDR < 0.05 and z-cutoff of ± 4, shown as dotted lines). (D) Gene enrichment for functional groups, determined by manual annotation, for "fast" (smaller $t_{1/2}$) and "slow" (larger $t_{1/2}$) hits.

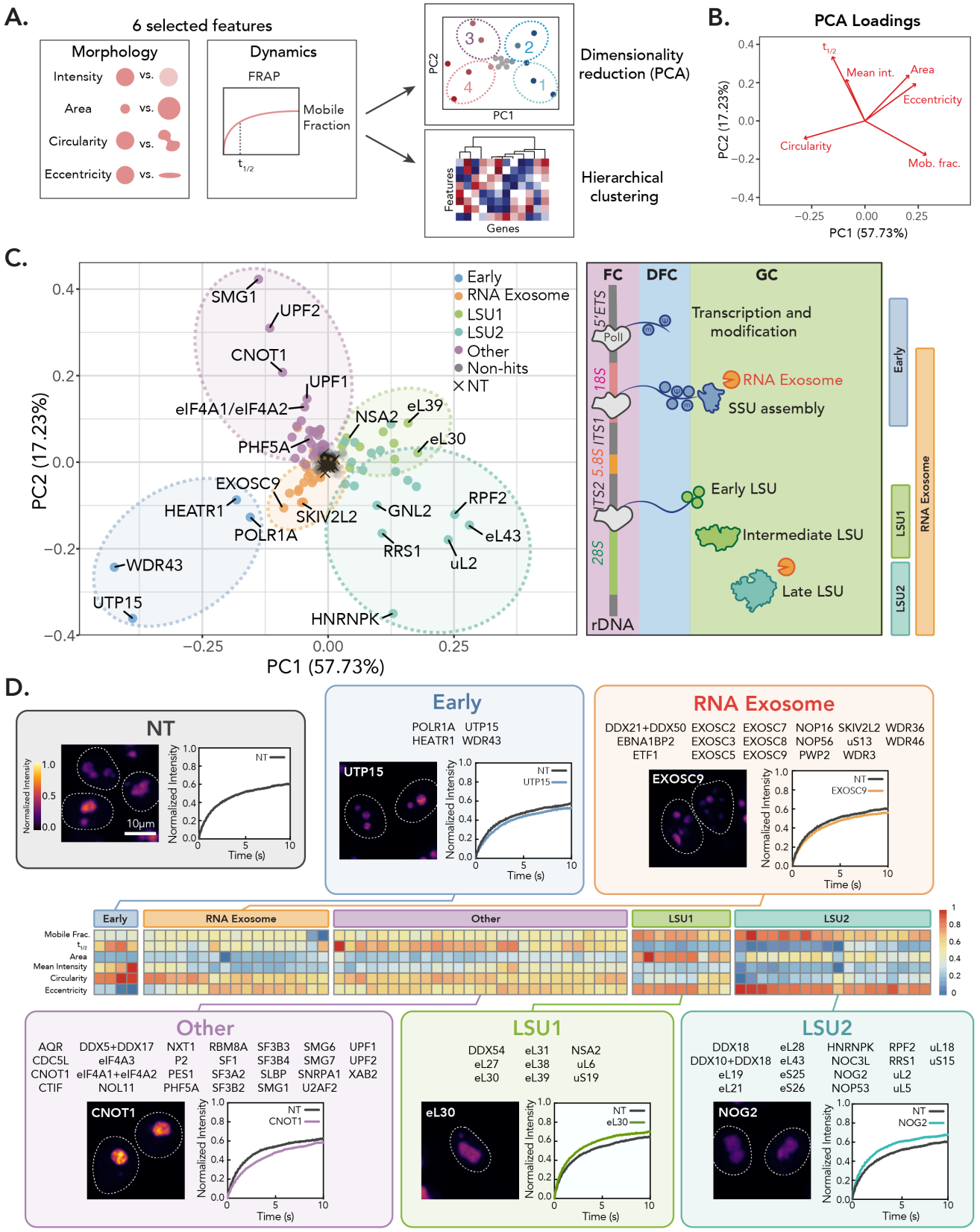
A.
6 selected features
Morphology
Intensity vs.
Area vs.
Circularity vs.
Eccentricity vs.
Dynamics
FRAP
Mobile Fraction
$t_{1/2}$
PC2
PC1
Dimensionality reduction (PCA)
Features
Genes
Hierarchical clustering
B.
PCA Loadings
$t_{1/2}$
Mean int.
Area
Eccentricity
Circularity
Mob. frac.
PC2 (17.23%)
PC1 (57.73%)
C.
Early
RNA Exosome
LSU1
LSU2
Other
Non-hits
NT
SMG1
UPF2
CNOT1
UPF1
eIF4A1/eIF4A2
NSA2
eL39
eL30
PHF5A
EXOSC9
HEATR1
SKIV2L2
GNL2
RPF2
POLR1A
eL43
RRS1
uL2
WDR43
UTP15
HNRNPK
PC2 (17.23%)
PC1 (57.73%)
FC
DFC
GC
5'ETS
18S
ITS1
5.8S
ITS2
28S
rDNA
Pol I
Transcription and modification
RNA Exosome
SSU assembly
Early LSU
Intermediate LSU
Late LSU
Early
LSU1
LSU2
RNA Exosome
D.
NT
Normalized Intensity
10μm
Time (s)
Early
POLR1A UTP15
HEATR1 WDR43
UTP15
RNA Exosome
DDX21+DDX50 EXOSC2 EXOSC7 NOP16 SKIV2L2 WDR36
EBNA1BP2 EXOSC3 EXOSC8 NOP56 uS13 WDR46
ETF1 EXOSC5 EXOSC9 PWP2 WDR3
EXOSC9
Mobile Frac.
Area
Mean Intensity
Circularity
Eccentricity
Other
AQR DDX5+DDX17 NXT1 RBM8A SF3B3 SMG6 UPF1
CDC5L eIF4A3 P2 SF1 SF3B4 SMG7 UPF2
CNOT1 eIF4A1+eIF4A2 PES1 SF3A2 SLBP SNRPA1 XAB2
CTIF NOL11 PHF5A SF3B2 SMG1 U2AF2
CNOT1
LSU1
DDX54 eL31 NSA2
eL27 eL38 uL6
eL30 eL39 uS19
eL30
LSU2
DDX18 eL28 HNRNPK RPF2 uL18
DDX10+DDX18 eL43 NOC3L RRS1 uS15
eL19 eS25 NOG2 uL2
eL21 eS26 NOP53 uL5
NOG2

Figure 3: Phenotype clustering identifies gene groups associated with specific nucleolar signatures. (A) Schematic overview of phenotypic clustering analysis (see also: Methods). (B) PCA loadings for each nucleolar feature. (C) PCA colored by phenotype cluster, as determined by hierarchical clustering shown in (D). Schematic of nucleolar ribosome biogenesis stages shown on right, with phenotypic classes associated with stages indicated. (D) Hierarchical clustering analysis for hits. Robust z-scores for all features were scaled from 0 to 1. Insets show image and representative FRAP curve for select hit in each phenotypic cluster. Images are scaled equally and colored with mpl-inferno LUT to show relative intensity differences. FRAP curve of NT control and gene depletion shown (n = 250 nucleoli, error bars are 95% CI).

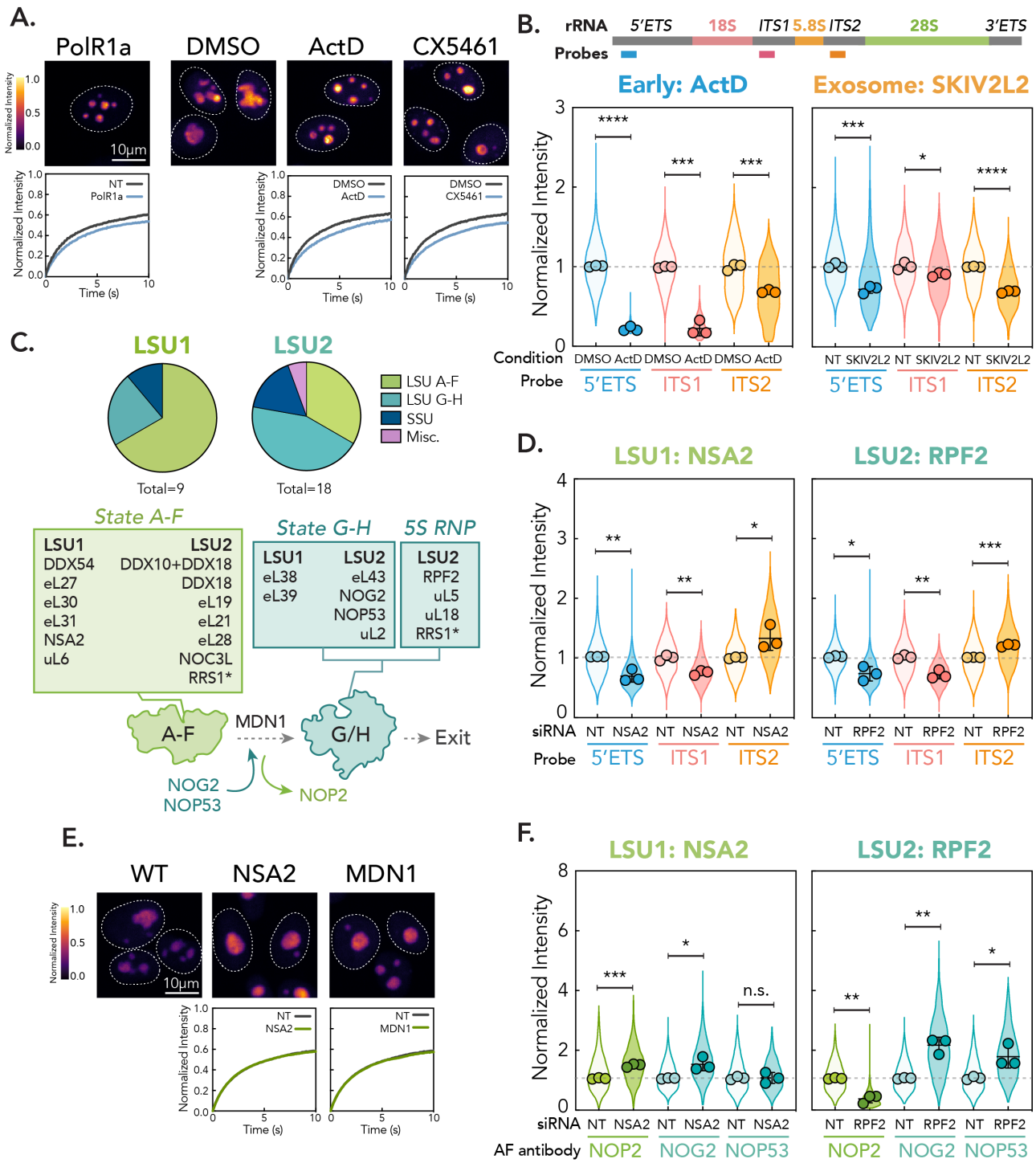

Figure 4: Distinct nucleolar phenotypes are associated with discrete stages in ribosome biogenesis. (A) Comparison between PolR1a knockdown (Early cluster) phenotype and treatment of cells with Pol I inhibitors (0.04 μg/mL ActD and 500 nM CX5461 for 2 hrs). Images are scaled equally and colored with mpl-inferno LUT to show relative intensity differences. FRAP curves for NT/vehicle control vs. gene depletion/drug shown (n = 250 nucleoli, error bars are 95% CI). (B) rRNA FISH for Early (ActD) and Exosome cluster (knockdown of SKIV2L2).

Schematic shows position of probes in 47S rRNA. Violin plots show spread of individual data points across three biological replicates (n = 600 nucleoli per replicate, points represent means of replicates, error bars are SD). The dotted line shows non-targeting control level. p-values calculated using two-tailed unpaired t-test between biological replicates. * $p < 0.05$, ** $p<0.01$, *** $p < 0.001$, **** $p<0.0001$. (C) Mapping genes in LSU1 and LSU2 phenotypic clusters onto LSU intermediates and schematic of State F to G transition. * = RRS1 associates in State A-F but is critical in 5S RNP recruitment. (D) rRNA FISH for representative hits in LSU1 (NSA2) and LSU2 (RPF2) gene clusters, as in (B). (E) Comparison of LSU1 cluster hit NSA2 and knockdown of MDN1. Images are scaled equally and colored with mpl-inferno LUT to show relative intensity differences. FRAP curves for NT vs. gene depletion shown (n = 250 nucleoli, error bars are 95% CI). (F) Nucleolar immunofluorescence of LSU intermediate markers for LSU1 and LSU2 representative gene hits. Three biological replicates were performed (n = 600 nucleoli per replicate, spread of individual nucleoli shown as violin, error bars are SD). Dotted line shows non-targeting control level. p-values calculated using two-tailed unpaired t-test between biological replicates. n.s. = not significant, * $p < 0.05$, ** $p<0.01$, *** $p < 0.001$.

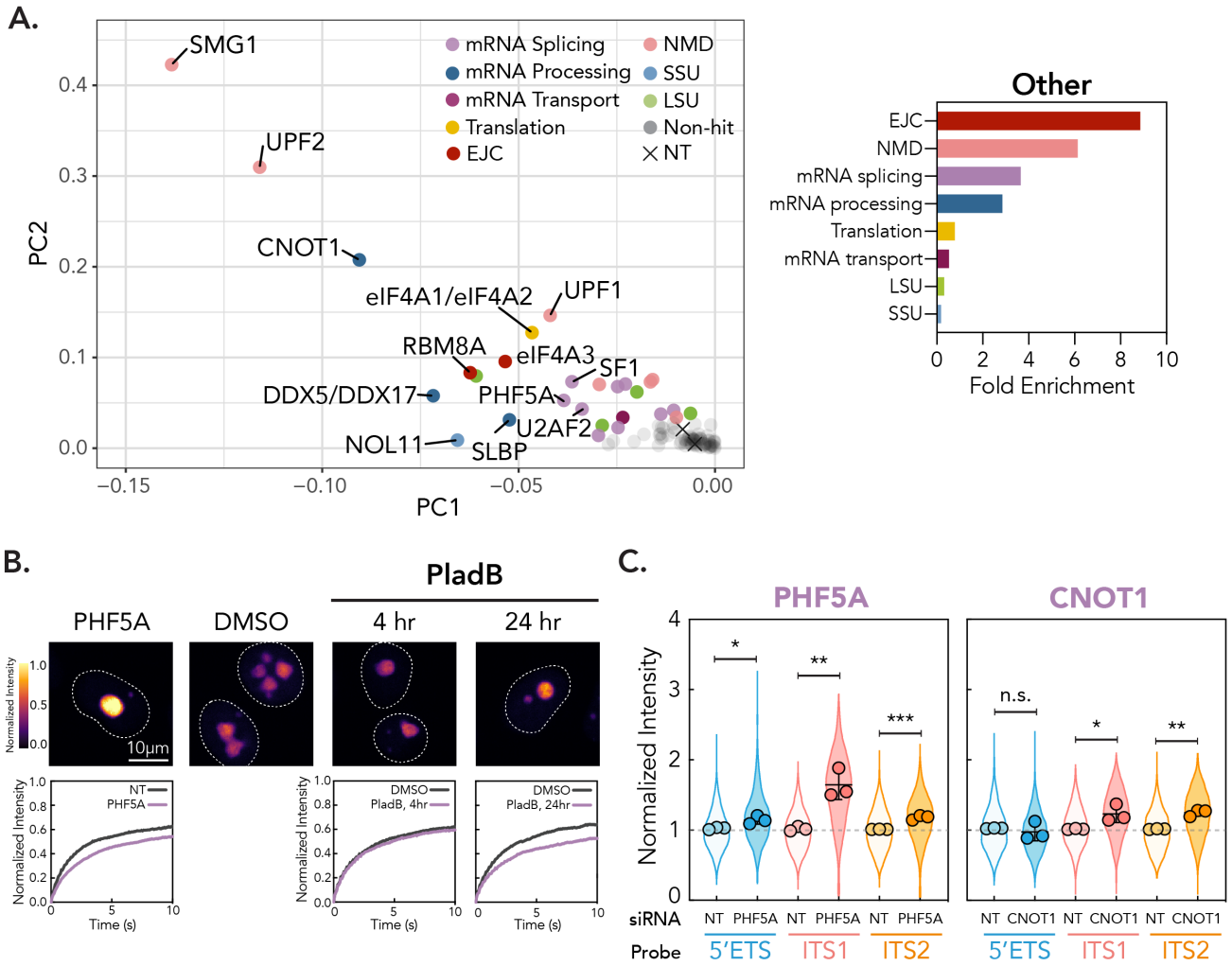

Figure 5: Disruption of mRNA splicing leads to slowed NPM1 dynamics and accumulation of rRNA precursors in the nucleolus. (A) "Other" phenotypic cluster shown as zoom of PCA in Fig. 3C. Fold enrichment for functional groups in "Other" cluster shown on right. (B) Comparison between "Other" representative hit PHF5A and treatment with splicing inhibitor PladB (10nM, for times shown). Images are scaled equally and colored with mpl-inferno LUT to show relative intensity differences. FRAP curves for NT/vehicle vs. gene depletion/PladB shown (n = 250 nucleoli, error bars are 95% CI). (C) rRNA FISH for representative gene hits in "Other" phenotypic cluster, as in Fig. 4B. n.s. = not significant, * $p < 0.05$, ** $p<0.01$, *** $p < 0.001$.

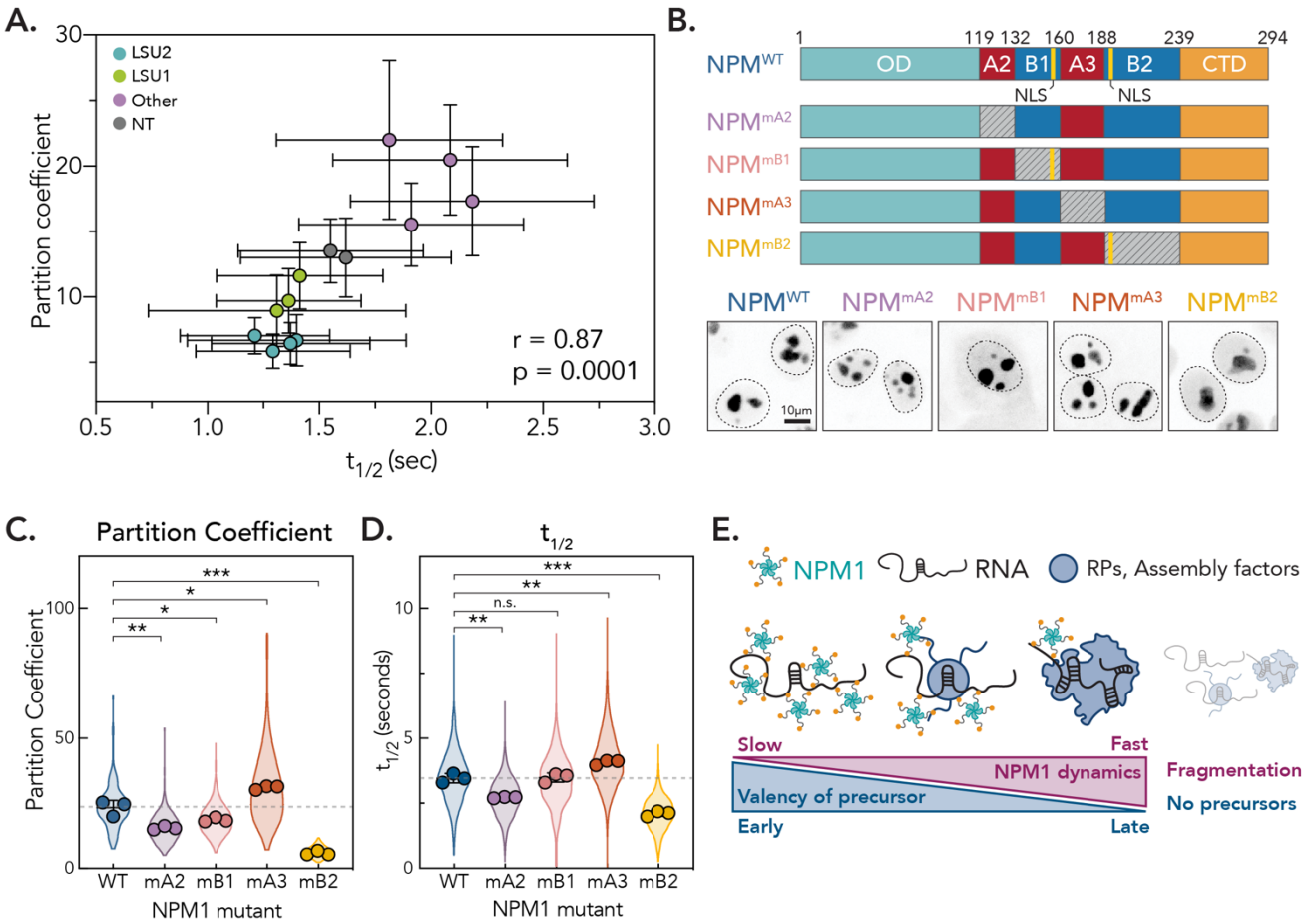

Figure 6: NPM1 dynamics are determined by interactions that drive partitioning into the nucleolus. (A) Partition coefficients vs. $t_{1/2}$ for representative hits in phenotypic clusters (n = 100 nucleoli, points are mean, error bars are SD). Pearson r and p-value indicated. (B) Schematic of NPM1 mutant constructs. Gray box represents charge neutralization. Yellow lines represent annotated nuclear localization signal (NLS). Representative images shown for localization pattern of each mutant construct. (C) Partition coefficients for each mutant construct. Violin shows spread of individual points for 3 biological replicates (n = 40 nucleoli per replicate, points show means of each replicate, error bars are SD). p-values calculated using two-tailed unpaired t-test between biological replicates. * $p < 0.05$, ** $p<0.01$, *** $p < 0.001$. (D) $t_{1/2}$ for each mutant construct. Violin shows spread of individual points for 3 biological replicates (n = 250 nucleoli per replicate, points show means of each replicate, error bars are SD). p-values calculated using two-tailed unpaired t-test between biological replicates. n.s. = not significant, ** $p<0.01$, *** $p < 0.001$. (E) Model for how valency of ribosome intermediates determine NPM1 dynamics.

Materials and Methods

Key resources table

Reagent or resource	Designation	Source or reference	Identifiers	Additional information
Cell line (human)	HeLa cell line with inducible Cas9 (cTT20.11)	Gift from Kara L. McKinley and Iain Cheeseman (McKinley and Cheeseman, 2017)	N/A	Parent cell line used for NPM1-tagged reporter cells
Cell line (human)	Lenti-X HEK 293T cells	Takara Biosciences	Cat# 632180	For lentivirus production.
Cell line (human)	NPM1-mNeonGreen HeLa	This paper	N/A	Tagged at endogenous locus.
Cell line (human)	NPM1-mScarlet HeLa	This paper	N/A	Tagged at endogenous locus.
Cell line (human)	NPM1^{WT}-mScarlet HeLa	This paper	N/A	
Cell line (human)	NPM1^{mA2}-mScarlet HeLa	This paper	N/A	
Cell line (human)	NPM1^{mB1}-mScarlet HeLa	This paper	N/A	
Cell line (human)	NPM1^{mA3}-mScarlet HeLa	This paper	N/A	
Cell line (human)	NPM1^{mB2}-mScarlet HeLa	This paper	N/A	
Construct/Plasmid	GFP-NPM WT	Gift from Xin Wang, (Wang. W et al., 2005)	Addgene # 17578	Used to obtain sequence of NPM1-WT.
Construct/Plasmid	pX330	Gift from Feng Zhang	Addgene # 42230	
Construct/Plasmid	pKLM73	Gift from Kara L. McKinley		Donor plasmid with C-terminal mNeonGreen and puromycin resistance cassette
Construct/Plasmid	pKLM110	Gift from Kara L. McKinley		Donor plasmid with C-terminal mScarlet and puromycin resistance cassette
Construct/Plasmid	pKLM79	Gift from Kara L. McKinley		Lentivirus transfer plasmid with C-terminal mScarlet Fusion tag. SFFV promoter. Used for NPM1 mutant constructs.
Construct/Plasmid	NPM1-mNeonGreen-Puro^{R} donor plasmid	This paper		

Construct/Plasmid	NPM1-mScarlet-Puro^{R} donor plasmid	This paper		
Construct/Plasmid	pX330-NPM1 sgRNA	This paper		Targeting sequence: GCCAGAGATCTTGAATAGCC
Construct/Plasmid	SFFV-NPM1^{WT}-mScarlet	This paper		
Construct/Plasmid	SFFV-NPM1^{mA2}-mScarlet	This paper		
Construct/Plasmid	SFFV-NPM1^{mB1}-mScarlet	This paper		
Construct/Plasmid	SFFV-NPM1^{mA3}-mScarlet	This paper		
Construct/Plasmid	SFFV-NPM1^{mB2}-mScarlet	This paper		
Software	μManager	Edelstein et al., 2014	Latest nightly build	https://micro-manager.org/
Software	Pycromanager	Pinkard, H. et al., 2021		https://github.com/micro-manager/pycro-manager/
Software	R	R Core Team, 2021	v. 4.1.1	https://www.r-project.org/
Software	Prism	GraphPad	v. 8.3.0	
Software	FIJI	Schindelin et al., 2012		https://imagej.net/software/fiji/
Software	CellProfiler	Stirling, D. R. et al., 2021	v.4.0.7	https://cellprofiler.org/
Oligonucleotide	5'ETS RNA FISH probe	Integrated DNA Technologies		Cy3-CGGAGGCCCAACCTCTCCGACGACAGGTCGCCAGAGGACAGCGTGTCAGC
Oligonucleotide	ITS1 RNA FISH probe	Integrated DNA Technologies		Cy3-CCTCGCCCTCCGGGCTCCGGGCTCCGTTAATGATC
Oligonucleotide	ITS2 RNA FISH probe	Integrated DNA Technologies		Cy3-CTGCGAGGGAACCCCCAGCCGCGCA
Oligonucleotide	SKIV2L2 ON-TARGETplus siRNA SMARTPool	Horizon Discovery	Cat # L-031902-02-0005	
Oligonucleotide	UPF1 ON-TARGETplus siRNA SMARTPool	Horizon Discovery	Cat # L-011763-00-0005	
Oligonucleotide	DDX54 ON-TARGETplus siRNA SMARTPool	Horizon Discovery	Cat # L-017128-01-0005	
Oligonucleotide	eIF4A3 ON-TARGETplus	Horizon Discovery	Cat # L-020762-00-0005	

	siRNA SMARTPool			
Oligonucleotide	NSA2 ON-TARGETplus siRNA SMARTPool	Horizon Discovery	Cat # L-017043-01-0005	
Oligonucleotide	MDN1 ON-TARGETplus siRNA SMARTPool	Horizon Discovery	Cat # L-009786-00-0005	
Oligonucleotide	RPF2 ON-TARGETplus siRNA SMARTPool	Horizon Discovery	Cat # L-024715-01-0005	
Oligonucleotide	GNL2 ON-TARGETplus siRNA SMARTPool	Horizon Discovery	Cat # L-020392-01-0005	
Oligonucleotide	PHF5A ON-TARGETplus siRNA SMARTPool	Horizon Discovery	Cat # L-014987-01-0005	
Oligonucleotide	CNOT1 ON-TARGETplus siRNA SMARTPool	Horizon Discovery	Cat # L-015369-01-0005	
Antibody	α-tubulin Monoclonal antibody (DM1A)	Invitrogen	Cat # 62204	
Antibody	eIF4A3 polyclonal antibody (Rabbit)	Proteintech	Cat 3 17504-1-AP	
Antibody	UPF1 (D15G6) Rabbit mAb	Cell Signaling Technology	Cat # 12040	
Antibody	SKIV2L2 polyclonal antibody (Rabbit)	Novus Biologicals	Cat # NB100-1574	
Antibody	DDX54 polyclonal antibody (Rabbit)	Proteintech	Cat # 26894-1-AP	
Antibody	NOL1 Antibody	Novus Biologicals	Cat # NBP1-92192	
Antibody	GNL2 Antibody	Novus Biologicals	Cat # NBP1-81649	
Antibody	GLTSCR2 Polyclonal Antibody	Proteintech	Cat # 27353-1-AP	
Antibody	Goat anti-Mouse IgG (H+L) Cross-Absorbed Secondary	Invitrogen	Cat # A-21235	

	Antibody, Alexa 647			
Antibody	Goat anti-Rabbit IgG (H+L) Cross-Absorbed Secondary Antibody, Alexa 647	Invitrogen	Cat # A-21245	
Antibody	Anti-mouse IgG, HRP-linked	Cell Signaling Technology	Cat # 7076S	
Antibody	Anti-Rabbit IgG (whole molecule)-Peroxidase antibody	Millipore	Cat # A0545-1ML	
Chemical	Actinomycin D	Sigma	Cat # A1410-2MG	
Chemical	CX-5461	SelleckChem	Cat # S2684	
Chemical	Pladienlolide B	Tocris	Cat # 6070	
Chemical	Hoechst 22242	ThermoFisher	Cat # H3570	
Chemical/Reagent	Lipofectamine LTX	ThermoFisher	Cat # 15338030	
Chemical/Reagent	Lipofectamine 2000	ThermoFisher	Cat # 11668027	
Chemical/Reagent	Lipofectamine RNAiMAX	ThermoFisher	Cat # 13778075	

Cell culture

HeLa (cTT20.11[66], gift from Kara L. McKinley and Iain Cheeseman) and Lenti-X HEK293T cells (Takara Bio, used for lentivirus production) were cultured in DMEM (Gibco) supplemented with 10% tetracycline-free FBS (Gemini) and penicillin and streptomycin (Gibco) at 37°C with 5% CO_2 in a humidified incubator. Cells were maintained at passage number under 25 and routinely checked for mycoplasma. Cells were passaged using 0.05% Trypsin-EDTA (Gibco).

Endogenously-tagged cell line generation

Endogenously-tagged cell lines were generated using CRISPR-Cas9 homology directed repair. A guide RNA targeting the last exon of NPM1 was designed using the Benchling CRISPR tool to maximize on-target and minimize off-target effects (targeting sequence: GCCAGAGATCTTGAATAGCC). This sequence was inserted into pX330 (gift of Feng Zheng, Addgene #42230), which encodes both spCas9 and the sgRNA. Homology arms for genes of interest were ordered from IDT as gBlocks with PAM sequence for sgRNA mutated. Homology arms were cloned into pKLM73 for mNeonGreen and pKLM110 for mScarlet (gifts from Kara L. McKinley) using NEBuilder HiFi DNA Assembly (New England Biolabs). To generate knock-in lines, HeLa cells were seeded in a 6-well plate at $1x10^6$ cells per well. The following day, cells were transfected with 1 μg each of the pX330 and donor plasmids using Lipofectamine 2000 (ThermoFisher). After 72 hours, cells were passaged into 10 cm dishes and cells with integration were selected for using puromycin at 1 μg/mL. After sufficient cell death and outgrowth of resistant colonies, cells were passaged one additional time to recover and then fluorescently positive cells were sorted for single cells into a 96-well plate using a Sony SH800 cell sorter. Single-cell clones were checked for correct localization of tagged protein and confirmed by genotyping PCR. Briefly, gDNA was isolated from a confluence 12-well plate by rinsing once with PBS followed by addition of 0.5 mL genomic DNA lysis buffer (100 mM Tris pH 8, 5mM EDTA, 200mM NaCl, 0.2% SDS, 0.2 mg/mL

proteinase K). Plates were incubated with lysis buffer at 37°C overnight. Lysed cells were transferred to an Eppendorf tube and DNA was precipitated using isopropanol followed by washing with 70% ethanol. Pellet was resuspended in TE buffer (1mM EDTA pH 8, 10mM Tris pH 8) and used as a template for amplification of insertion regions. Products were visualized for size differences by agarose gel and then gel purified and submitted for Sanger sequencing.

Microscopy

All live-cell and fixed-cell confocal imaging was carried out on a Nikon Ti-E inverted microscope equipped with a Yokogawa CSU-X high-speed confocal scanner unit and a pair of Andor iXon 512 × 512 EMCCD cameras. All components of the microscope were controlled by the open-source platform μManager[67]. The microscope stage was enclosed in a custom-built incubator that maintains preset temperature. Live-cell imaging was performed at 37°C with 5% CO_2 and cells were equilibrated on the microscope for at least 30 minutes prior to imaging. Fixed-cell imaging was performed at room temperature. High-magnification images were obtained using a 100x 1.49 NA oil-immersion objective. HiT-FRAP and high-content images were acquired with a 40x 0.95 NA air objective. For HiT-FRAP, images for mNeonGreen cells and mScarlet cells were collected at 100x EM gain with a 50 ms and 100 ms exposure, respectively. Bleaching was performed with a 405 nm focused laser beam set at 10 mW power steered by a pair of galvo mirrors (Rapp UGA-40), which was controlled by the Projector Plugin in μManager.

HiT-FRAP acquisition

Automated FRAP experiments were performed using custom code and the Python library Pycromanager[68], which integrates hardware control with image processing via μManager. Image processing was performed using scikit-image[69]. Positions and wells for acquisition were defined using the μManager High Content Screening (HCS) Site Generator Plugin. Exposure length was predetermined for each cell line to avoid saturated pixels. HiT-FRAP acquisition proceeded as follows: at each field of view, a single image was acquired. Organelles of interest were then identified. Firstly, the background pixel threshold was determined using Otsu's method. Threshold values for nucleoli were determined using local thresholding, and regions larger than 1000 pixels were removed. Both thresholds were combined and then subjected to two rounds of erosion and dilation, followed by removal of objects smaller than 10 pixels to clear the background. To maximize throughput, further analysis and acquisition only continued if greater than 20 organelles were present in a field of view. Centroids for organelles were then determined to generate a bleach position list. We set a size threshold for bleached organelles of at least twice the area of the bleach spot to preferentially capture internal mixing rather than exchange with the nucleoplasm, although due to limitations in magnification and the fixed size of our bleach laser, whole-organelle bleaches could not be completely avoided. A random 50% of these positions were then chosen for bleaching, with the remainder kept as controls to account for acquisition photobleaching. Bleach locations were exported for every field of view to be used in post-analysis. Acquisition then started, followed by concurrent bleaching at designated organelle centroid positions. Length of acquisition was manually pre-determined to achieve recovery plateau. This process was iterated through multiple fields of view until 500 bleaches were acquired, after which the stage was moved to the next well and the sequence repeated.

To account for drift in the bleach laser position, automated recalibration was performed as follows: after every two fields of view, a single image was acquired. The image was thresholded to identify cells using the triangle algorithm, and a position closest to the center that did not have a foreground object (cell) was determined. The bleach laser was then targeted to this location and an image was taken of the exposure. The true bleach laser position was determined from this image by identifying the maximum intensity position in the image. To increase the speed of finding this location, a region of interest was used based upon the estimated location of the bleach laser. When the square of the distance between the intended target and the true bleach spot location was greater than an offset of 5, a full calibration of the laser was performed.

HiT-FRAP image analysis

Analysis of high-content FRAP data was performed using the same software used for acquisition. For each FRAP recovery time series, nucleoli were identified in frame 0 using the same thresholding procedure as used for acquisition. Bleach spots were then identified as follows: the bleach positions generated during acquisition (pointers) were linked to the bleach frame. To account for experimental offsets in bleach positions, true bleach locations were determined empirically. Briefly, it was manually determined that the minimum intensity post-reported bleach time occurred after four frames (bleach time offset). For each pointer position, the minimum intensity frame (bleach frame + bleach time offset) was subtracted from the bleach frame and smoothed to remove background noise. Otsu global thresholding was then applied to identify bright spots (detected bleach spots). After two rounds of erosion and dilation to minimize background noise, the centroids of the closest detected bleach spots to each original pointer position were used as the true bleach location. These true bleach coordinates were then linked to the corresponding organelle. Bleach spots that fall outside of a nucleolus, bleach the same nucleolus, overlap, or are too far away from the original pointer position (>20 pixels in any direction) were filtered. Bleach spot masks were then generated by subjecting the true bleach coordinates to three rounds of dilation.

Using these bleach spot masks, FRAP curves were determined as follows: to monitor photobleaching due to acquisition, control spot masks were generated by identifying centroids of unbleached organelles and submitting these to three rounds of dilation. Raw intensities for the bleach and control spots were calculated over the time course. Background was determined for each frame by generating a binary image of regions with a pixel intensity of less than 300, removing regions smaller than 50 pixels. The mean intensity of the largest area was used as background and subtracted from all measured intensities. A photobleaching factor was then determined for control spots and calculated as the intensity ratio between the control spot at every time point as compared to intensity at $t = 0$. The mean of this ratio across all control spots was then used as a correction factor for bleach spot intensities. These intensities were then normalized to the pre-bleach intensity and minimium intensity (0 to 1) to generate final intensities for fitting. These intensities were then fit to several FRAP models (single exponential, double exponential, soumpasis, and ellenberg), although single exponential fittings were used in all subsequent analyses. Curves were filtered out if they had less than 5 frames prior to bleach (to avoid poor determination of pre-bleach intensity), imaged for less than 100 frames post bleach for mNeonGreen or 50 frames for mScarlet (to ensure adequate recovery), if the mobile fraction was less than 0 or greater than 1.05, and if $R^2 < 0.7$. Parameters from the fitted curve are then exported (initial slope, mobile fraction, and $t_{1/2}$).

Organelle features were determined as follows: for each bleached nucleolus, the following organelle features available in scikit-image were calculated: area, mean intensity, circularity, eccentricity, solidity, minimum intensity, maximum intensity, perimeter, hu moments (2nd, 3rd, and 4th), intensity percentiles (1st, 5th, 95th, and 99th), median intensity, the standard deviation of intensities, intensity kurtosis, and intensity skew.

Dynamics screen phenotype analysis

Gene depletions with high cell death were removed manually from all subsequent analysis (DDX19B, DDX19A+DDX19B, DDX39A+DDX39B, and SNRNP200, CRNKL2, CWC22, EFTUD3, eS4, eS6, PRPF8, SNW1). Dynamics features (mobile fraction and $t_{1/2}$) were normalized using the median and median absolute deviation for all non-targeting siRNA controls in the same plate to account for plate-to-plate variation (robust z-score). Medians of robust z-scores were computed and used in final hit calling. p-values were calculated using the Kolmogorov-Smirnov test as compared to a randomly chosen subset (10%) of non-targeting control wells. FDR was determined using the Benjamini-Hochberg procedure. As indicated in the figure legends, an FDR threshold of 0.05 was used for defining significance. Thresholds for z-scores were set as indicated in figure legends.

Principal component analysis for multidimensional analysis

Phenotype scores were calculated and incorporate the -ln(p-value) (determined by Kolmogorov-Smirnov test) and effect size as compared to a subset (randomly selected 10%) of non-targeting control wells in the same

plate to account for plate-to-plate variation. The remainder of non-targeting controls were treated as experimental samples to test the robustness of the scoring method. Phenotype scores were scaled from 0 to 1 prior to further analysis. PCA was performed using the prcomp R package. The R packages ggplot2[70], ggfortify[71], and ggrepel[72] were used to generate figures and are available through CRAN. Hits were manually called by separation from NT control cluster.

Hierarchical clustering to identify phenotype clusters

Robust z-scores for hits were used in hierarchical clustering using the pheatmap R package[73] by Euclidean distance and complete agglomeration. The resulting dendrogram was split into subtrees until clusters represented similar overall trends, generating the five phenotypic clusters shown in Fig. 3.

Cloning for mutant NPM1 lentivirus constructs

All constructs were cloned into the lentiviral transfer plasmid pKLM79 (gift of Kara L. McKinley), which contains a C-terminal mScarlet fusion tag. The wild-type sequence of NPM1 was cloned from GFP-NPM WT (gift from Xin Wang, Addgene plasmid # 17578). Mutant NPM1 plasmids were constructed by ordering mutated regions as gBlocks from IDT with overhangs complementary to proximal regions. Proximal regions were then amplified from the wild-type construct to generate fragments with appropriate overhangs for assembly by NEBuilder HiFi DNA Assembly (New England Biolabs) into pKLM79 (cut with MluI and SpeI, New England Biolabs).

Lentivirus transduction

Lentiviral particles were packaged by transfecting Lenti-X 293T cells with transfer construct of interest and PSP and VSVG helper plasmids using Lipofectamine LTX (Thermo Fisher) reagent. Media was changed 18 hours later and virus was harvested 72hrs after transfection. Virus was cleared by passing through a 0.45 μm PVDF filter. 200μL viral supernatant was used to transduce a 6-well plate of HeLa cells by spinfection. Briefly, cells were seeded in suspension at 250,000 cells per well in the presence of viral supernatant and polybrene (Sigma-Aldrich) at a final concentration of 10μg/mL. Cells were spun at 1000 x g for 45 minutes at 37°C and allowed to recover overnight. Media was replaced the following day and transduction was allowed to proceed for 48 hours until passage. Cells were passaged for at least two passages to eliminate cells that exhibited toxic levels of expression. Fluorescent cells were sorted using a Sony SH800 cell sorter gated to select the top 40% of expressing cells. Polyclonal populations were used for all experiments.

siRNAs

For the primary RNA helicase and secondary screen, candidate libraries of ON-TARGETplus SMARTPool siRNAs (4 guides per gene) were ordered in arrayed format from Horizon Discovery. Non-targeting siRNA pools were interspersed randomly throughout the plate at a ratio of 1:6 to on-target pools. For depooled validation, deconvoluted guide pools (single guides) were ordered in an arrayed format for select hits. Single non-targeting guides were interspersed randomly throughout the plate at a ratio of 1:6. For knockdown of single genes, ON-TARGETplus siRNA pooled guides were ordered from Horizon Discovery (see Key Resources Table).

siRNA transfections

For screens and depooled validation experiments, siRNAs were reverse transfected at a final concentration of 5nM using Lipofectamine RNAiMAX reagent (Life Technologies). Briefly, siRNA:lipid mixes were pipetted into wells of a 384-well glass bottom dishes (Matriplate; Brooks). After a 15-minute incubation, cells were seeded at 900 cells per well. Knockdown was allowed to proceed for 72 hours before imaging. For validation experiments (RNA FISH, IF, and single gene knockdowns), pooled guide RNAs were reverse transfected at a final concentration of 25nM into 96-well glass-bottom imaging plates (Matriplate; Brooks), with cells seeded at a density of 8000 cells per well. For qPCR and westerns, cells were reverse transfected with pooled guide RNAs at a final concentration of 25nM into 24-well tissue culture dishes (Corning) and cells were plated at 24,000 cells per well.

Drug treatments
For all drug treatments, cells were seeded at 50,000 cells per well into 96-well glass bottom imaging dishes (Matriplate; Brooks) 24 hours prior to experiments. For ATP depletion, cells were washed twice in DMEM without glucose (Gibco) and then incubated for 10 minutes with 10 mM sodium azide and 6mM 2-deoxyglucose diluted in DMEM without glucose supplemented with 10% tetracycline free FBS (Gemini). For Pol I inhibitors, cells were treated with 0.04 μg/mL actinomycin D (Sigma) or 500 nM CX5461 (SelleckChem) diluted in culture media for 2 hours. For pladienolide B treatment, cells were treated with 10 nM PladB (Tocris) diluted in culture media for indicated times. For all imaging experiments, cells were transferred to heated and equilibrated microscope at least 30 minutes prior to imaging.

RNA fluorescent in situ hybridization (RNA FISH)
RNA FISH was performed in a 96-well plate format (see siRNA transfections). After knockdown or drug treatment, cells were fixed in 4% Paraformaldehyde in PBS at 37°C for 10 minutes. Cells were then permeabilized by incubation with ice-cold methanol at -20°C for 10 minutes. Cells were incubated with 1M Tris pH 8 for approximately 10 minutes. 5' Cy5 labeled DNA probes (see Supplementary Table 1) were ordered from IDT and resuspended at 1 μg/mL in water. Stock probes were diluted 1:1000 in RNA FISH hybridization buffer preheated to 42°C (15% deionized formamide, 10% dextran sulfate, 2x SSC from Ambion, 0.02% BSA, 0.2mg/mL Baker's yeast tRNA from Ambion). Plate was placed in plastic bag with wet paper towels and incubated at 42°C for 1 hour. Cells were washed with 2x SSC three times at room temperature, followed by incubation with Hoechst 33342 DNA dye diluted at 1:1000 in 2x SSC for 10 minutes at room temperature. Cells were washed a final three times with 2x SSC and then imaged.

Immunofluorescence (IF)
Immunofluorescence was performed in 96-well plate format (see siRNA transfections). After knockdown or drug treatment, cells were fixed in 4% Paraformaldehyde in PBS at 37°C for 10 minutes. Cells were then permeabilized by incubation with ice-cold methanol at -20°C for 10 minutes. Fixed cells were blocked in 3% BSA in PBST (PBS from Gibco supplemented with 0.1% Tween-20) for at least 1 hour, followed by incubation overnight with primary antibodies diluted at 1:500 in antibody dilution buffer (3% BSA, PBST, 0.02% sodium azide). The following day, cells were washed three times with PBST followed by incubation for 1-2 hrs at room temperature with appropriate secondary antibody conjugated to Alexa 647 (ThermoFisher) diluted at 1:1000 in antibody dilution buffer. Cells were then washed three times with PBST and incubated with Hoechst 33342 DNA dye (Invitrogen) diluted at 1:1000 for 10 minutes at room temperature. Cells were washed a final three times with PBST and then imaged.

RT-qPCR
Cells were transfected in 24-well format, see siRNA transfection protocol above. After 72 hours of gene knockdown, cells were rinsed twice with ice-cold PBS (Gibco) and then scraped into 200 μL TRIzol Reagent (Invitrogen) and lysed by pipetting. Lysed cells were incubated for 5 minutes at room temperature. 40 μL chloroform was added and tubes were mixed by inversion followed by incubation for 2 minutes at room temperature. Samples were centrifuged for 15 minutes at 12,000 x g at 4°C. The aqueous phase was transferred to a new tube. RNA was extracted using Zymo RNA Clean and Concentrator kit according to manufacturer's protocol. RNA was eluted in 15 μL RNase-free water (Ambion). cDNA was generated from 1 μg total RNA using iScript cDNA Synthesis Master Mix (Bio-Rad). cDNA was then diluted 1:20 for rRNA intermediates and 1:100 for mature rRNAs. RT-qPCR was performed using SYBR Green PCR Master Mix (Applied Bioystems) according to manufacturer's protocol with a Bio-Rad CFX 96 Real Time thermal cycler. Reactions were run in technical triplicate and GAPDH was used as a housekeeping gene with the following primers:
GAPDH-F (5'-GTCTCCTCTGACTTCAACAGCG-3')
GAPDH-R (5'-ACCACCCTGTTGCTGTAGCCAA-3')
Primers used to amplify rRNA regions were as follows:
47S-F (5'-GAACGGTGGTGTGTCGTT-3')

47S-R (5'-GCGTCTCGTCTCGTCTCACT-3')
18S_5'-F (5'-GCCGCGCTCTACCTTACCTACCT-3')
18S_5'-R (5'-CAGACATGCATGGCTTAATCTTTG-3')
18S_3'-F (5'-AGTCGTAACAAGGTTTCCGTAGGT-3')
18S_3'-R (5'-CCTCCGGGCTCCGTTAAT-3')
5.8S_5'-F (5'-TACGACTCTTAGCGGTGGATCA-3')
5.8S_5'-R (5'-TCACATTAATTCTCGCAGCTAGCT-3')
5.8S_3'-F (5'-GAATTGCAGGACACATTGATCATC-3')
5.8S_3'-R (5'-GGCAAGCGACGCTCAGA-3')
18S-F (5'-CTGGATACCGCAGCTAGGAA-3')
18S-R (5'-GAATTTCACCTCTAGCGGCG-3')
5.8S-F (5'-ACTCGGCTCGTGCGTC -3')
5.8S-R (5'-GCGACGCTCAGACAGG-3')
28S-F (5'-CGGCGGGAGTAACTATGACT-3')
28S-R (5'-GCTGTGGTTTCGCTGGATAG-3').

Western blotting

Cells were washed twice with ice-cold PBS and then scraped into RIPA buffer (ThermoFisher) supplemented with protease inhibitors (cOmplete Mini Tablets, Roche). Cells were lysed by with a probe sonicator at 20% power in two 30-second intervals on ice. Lysates were normalized by OD_{260} and denatured in sample buffer and boiled for 5 minutes at 95°C. Samples were run on a 4-20% Mini-PROTEAN TGX precast gel (Bio-Rad) and then transferred to nitrocellulose using a Bio-Rad TransBlot Turbo system. Membranes were blocked in 3% w/v BSA in TBST (50 mM Tris pH 8, 150 mM NaCl, 0.1% TWEEN-20) for 30 minutes and then incubated with primary antibodies overnight diluted at 1:1000 in antibody dilution buffer (3% BSA in TBST with 0.02% sodium azide). Membranes were washed three times in TBST and then incubated in 1:10,000 secondary antibody diluted in 3% BSA in TBST for 1-2 hours. Membranes were again washed three times in TBST and then incubated in SuperSignal West Pico Plus ECL substrate (ThermoFisher) and imaged on a Bio-Rad ChemiDOC MP Imaging system.

Quantification of nucleolar RNA FISH and IF

Fixed-cell images were analyzed using custom pipelines developed in CellProfiler[74] (v.4.0.7). Briefly, for nucleolar RNA FISH, nucleoli were segmented using the NPM1-tagged channel using adaptive Otsu thresholding. There is a higher nucleoplasmic signal for FISH samples, and therefore, three threshold classes were used and the bottom two were classified as background. The object diameter range was set to 10-300 pixels, and objects outside this range were discarded. Nucleoli that touch the border of the image were discarded. Identified nucleoli were shrunk but 1 pixel to eliminate impacts of edge effects on intensity measurements. Intensity of identified nucleoli objects were measured for both the unscaled NPM1-tagged channel and the stained channel. For IF, the same pipeline was used, but nucleoli were thresholded using two class thresholding. A custom Python script was used for post-processing of CellProfiler data to bin images by field of view and experimental condition. In addition, nucleoli that had an NPM1 intensity level of less than 0.01 were eliminated to omit fields of view with no cells, which resulted in inappropriate identification of background noise.

Partition coefficient calculations

Partition coefficients were determined manually by quantifying relative nucleolar (I^{dense}) and nucleoplasmic (I^{dilute}) NPM1 intensities from pre-bleach (time point 0) images acquired by HiT-FRAP, as follows: Nucleolar signal was determined by measuring the average intensity of a 10 x 10 pixel box in the most intense region of nucleolar signal (5 x 5 pixels were used when nucleoli were small). Nucleoplasmic signal was determined by measuring the average intensity of a 10 x 10 pixel box that was manually chosen in the same cell as the measured nucleolus. Background was determined by averaging the average intensity across 5 randomly

chosen 10 x 10 pixel locations. Background was subtracted, and then the ratio of nucleolar to nucleoplasmic signals were calculated to determine partition coefficient ($K = I^{dense}/I^{dilute}$, where K = partition coefficient).

RNA Helicase phylogenetic analysis

Full-length, reference protein sequences for indicated DEAD-box proteins were retrieved from NCBI and aligned using MUSCLE[75]. A maximum-likelihood tree was constructed using MEGA[76] using default options and the JTT model.

Statistical analysis

Software used for statistical analysis of screen-related data is listed in subsection of methods above. Otherwise, all other statistical tests were performed in Prism 8 as indicated in figure legends.

References

1. Donati, G., Montanaro, L. & Derenzini, M. Ribosome Biogenesis and Control of Cell Proliferation: p53 Is Not Alone. *Cancer Research* **72**, 1602–1607 (2012).
2. Lempiäinen, H. & Shore, D. Growth control and ribosome biogenesis. *Current Opinion in Cell Biology* **21**, 855–863 (2009).
3. Golomb, L., Volarevic, S. & Oren, M. p53 and ribosome biogenesis stress: The essentials. *FEBS Letters* **588**, 2571–2579 (2014).
4. Klinge, S. & Woolford, J. L. Ribosome assembly coming into focus. *Nat Rev Mol Cell Biol* **20**, 116–131 (2019).
5. Parker, M. D. & Karbstein, K. Quality control ensures fidelity in ribosome assembly and cellular health. *Journal of Cell Biology* **222**, e202209115 (2023).
6. Krüger, T., Zentgraf, H. & Scheer, U. Intranucleolar sites of ribosome biogenesis defined by the localization of early binding ribosomal proteins. *Journal of Cell Biology* **177**, 573–578 (2007).
7. Lafontaine, D. L. J., Riback, J. A., Bascetin, R. & Brangwynne, C. P. The nucleolus as a multiphase liquid condensate. *Nat Rev Mol Cell Biol* **22**, 165–182 (2021).
8. Boisvert, F.-M., van Koningsbruggen, S., Navascués, J. & or, A. I. The multifunctional nucleolus. *Nat Rev Mol Cell Biol* **8**, 574–585 (2007).
9. Hernandez-Verdun, D., Roussel, P., Thiry, M., Sirri, V. & Lafontaine, D. L. J. The nucleolus: structure/function relationship in RNA metabolism. *Wiley Interdiscip Rev RNA* **1**, 415–431 (2010).
10. Mitrea, D. M. *et al.* Nucleophosmin integrates within the nucleolus via multi-modal interactions with proteins displaying R-rich linear motifs and rRNA. *eLife* **5**, e13571 (2016).
11. LaPeruta, A. J., Micic, J. & Woolford Jr., J. L. Additional principles that govern the release of pre-ribosomes from the nucleolus into the nucleoplasm in yeast. *Nucleic Acids Research* gkac430 (2022) doi:10.1093/nar/gkac430.
12. Riback, J. A. *et al.* Composition-dependent thermodynamics of intracellular phase separation. *Nature* **581**, 209–214 (2020).
13. Feric, M. *et al.* Coexisting Liquid Phases Underlie Nucleolar Subcompartments. *Cell* **165**, 1686–1697 (2016).
14. Brangwynne, C. P., Mitchison, T. J. & Hyman, A. A. Active liquid-like behavior of nucleoli determines their size and shape in Xenopus laevis oocytes. *Proceedings of the National Academy of Sciences* **108**, 4334–4339 (2011).
15. Zhu, L. *et al.* Controlling the material properties and rRNA processing function of the nucleolus using light. *PNAS* **116**, 17330–17335 (2019).
16. Ogawa, L. M. *et al.* Increased numbers of nucleoli in a genome-wide RNAi screen reveal proteins that link the cell cycle to RNA polymerase I transcription. *Mol Biol Cell* **32**, 956–973 (2021).
17. Farley-Barnes, K. I. *et al.* Diverse Regulators of Human Ribosome Biogenesis Discovered by Changes in Nucleolar Number. *Cell Reports* **22**, 1923–1934 (2018).
18. Nicolas, E. *et al.* Involvement of human ribosomal proteins in nucleolar structure and p53-dependent nucleolar stress. *Nat Commun* **7**, 11390 (2016).

19. Negi, S. S. & Olson, M. O. J. Effects of interphase and mitotic phosphorylation on the mobility and location of nucleolar protein B23. *Journal of Cell Science* **119**, 3676–3685 (2006).
20. Caragine, C. M., Haley, S. C. & Zidovska, A. Nucleolar dynamics and interactions with nucleoplasm in living cells. *eLife* **8**, e47533 (2019).
21. Hondele, M. *et al.* DEAD-box ATPases are global regulators of phase-separated organelles. *Nature* **573**, 144–148 (2019).
22. Overwijn, D. & Hondele, M. DEAD-box ATPases as regulators of biomolecular condensates and membrane-less organelles. *Trends in Biochemical Sciences* **48**, 244–258 (2023).
23. Linsenmeier, M. *et al.* Dynamic arrest and aging of biomolecular condensates are modulated by low-complexity domains, RNA and biochemical activity. *Nat Commun* **13**, 3030 (2022).
24. Mitterer, V. & Pertschy, B. RNA folding and functions of RNA helicases in ribosome biogenesis. *RNA Biol* **19**, 781–810.
25. Dembowski, J. A., Kuo, B. & Woolford, J. L. Has1 regulates consecutive maturation and processing steps for assembly of 60S ribosomal subunits. *Nucleic Acids Res* **41**, 7889–7904 (2013).
26. Burger, F., Daugeron, M.-C. & Linder, P. Dbp10p, a putative RNA helicase from Saccharomyces cerevisiae, is required for ribosome biogenesis. *Nucleic Acids Res* **28**, 2315–2323 (2000).
27. Choudhury, P., Kretschmer, J., Hackert, P., Bohnsack, K. E. & Bohnsack, M. T. The DExD box ATPase DDX55 is recruited to domain IV of the 28S ribosomal RNA by its C-terminal region. *RNA Biology* **18**, 1124–1135 (2021).
28. Chlon, T. M. *et al.* Germline DDX41 mutations cause ineffective hematopoiesis and myelodysplasia. *Cell Stem Cell* **28**, 1966-1981.e6 (2021).
29. Kanellis, D. C. *et al.* The exon-junction complex helicase eIF4A3 controls cell fate via coordinated regulation of ribosome biogenesis and translational output. *Sci Adv* **7**, eabf7561 (2021).
30. de Planell-Saguer, M., Schroeder, D. G., Rodicio, M. C., Cox, G. A. & Mourelatos, Z. Biochemical and genetic evidence for a role of IGHMBP2 in the translational machinery. *Human Molecular Genetics* **18**, 2115–2126 (2009).
31. Jalal, C., Uhlmann-Schiffler, H. & Stahl, H. Redundant role of DEAD box proteins p68 (Ddx5) and p72/p82 (Ddx17) in ribosome biogenesis and cell proliferation. *Nucleic Acids Res* **35**, 3590–3601 (2007).
32. Bohnsack, K. E., Yi, S., Venus, S., Jankowsky, E. & Bohnsack, M. T. Cellular functions of eukaryotic RNA helicases and their links to human diseases. *Nat Rev Mol Cell Biol* (2023) doi:10.1038/s41580-023-00628-5.
33. Szklarczyk, D. *et al.* The STRING database in 2023: protein-protein association networks and functional enrichment analyses for any sequenced genome of interest. *Nucleic Acids Res* **51**, D638–D646 (2023).
34. Dash, S. *et al.* rRNA transcription is integral to phase separation and maintenance of nucleolar structure. *PLOS Genetics* **19**, e1010854 (2023).

35. Perry, R. P. & Kelley, D. E. Inhibition of RNA synthesis by actinomycin D: Characteristic dose-response of different RNA species. *Journal of Cellular Physiology* **76**, 127–139 (1970).
36. Perry, R. P. & Kelley, D. E. Persistent synthesis of 5S RNA when production of 28S and 18S ribosomal RNA is inhibited by low doses of actinomycin D. *Journal of Cellular Physiology* **72**, 235–245 (1968).
37. Drygin, D. *et al.* Targeting RNA polymerase I with an oral small molecule CX-5461 inhibits ribosomal RNA synthesis and solid tumor growth. *Cancer Res* **71**, 1418–1430 (2011).
38. Zinder, J. C. & Lima, C. D. Targeting RNA for processing or destruction by the eukaryotic RNA exosome and its cofactors. *Genes Dev.* **31**, 88–100 (2017).
39. Thoms, M. *et al.* The Exosome Is Recruited to RNA Substrates through Specific Adaptor Proteins. *Cell* **162**, 1029–1038 (2015).
40. Gallagher, J. E. G. *et al.* RNA polymerase I transcription and pre-rRNA processing are linked by specific SSU processome components. *Genes Dev.* **18**, 2506–2517 (2004).
41. Broeck, A. V. & Klinge, S. Principles of human pre-60S biogenesis. 2023.03.14.532478 Preprint at https://doi.org/10.1101/2023.03.14.532478 (2023).
42. Leidig, C. *et al.* 60S ribosome biogenesis requires rotation of the 5S ribonucleoprotein particle. *Nat Commun* **5**, 3491 (2014).
43. Micic, J. *et al.* Coupling of 5S RNP rotation with maturation of functional centers during large ribosomal subunit assembly. *Nat Commun* **11**, 3751 (2020).
44. Khatter, H., Myasnikov, A. G., Natchiar, S. K. & Klaholz, B. P. Structure of the human 80S ribosome. *Nature* **520**, 640–645 (2015).
45. Kater, L. *et al.* Visualizing the Assembly Pathway of Nucleolar Pre-60S Ribosomes. *Cell* **171**, 1599-1610.e14 (2017).
46. Kawashima, S. A. *et al.* Potent, Reversible, and Specific Chemical Inhibitors of Eukaryotic Ribosome Biogenesis. *Cell* **167**, 512-524.e14 (2016).
47. Kotake, Y. *et al.* Splicing factor SF3b as a target of the antitumor natural product pladienolide. *Nat Chem Biol* **3**, 570–575 (2007).
48. Ferrolino, M. C., Mitrea, D. M., Michael, J. R. & Kriwacki, R. W. Compositional adaptability in NPM1-SURF6 scaffolding networks enabled by dynamic switching of phase separation mechanisms. *Nat Commun* **9**, 5064 (2018).
49. Laperuta, A. Pre-ribosomes Release from the Nucleolus when They Lose Trans Interactions Through Changes in Protein Composition and rRNA Compaction. (Carnegie Mellon University, 2022). doi:10.1184/R1/19650522.v1.
50. White, M. R. *et al.* C9orf72 Poly(PR) Dipeptide Repeats Disturb Biomolecular Phase Separation and Disrupt Nucleolar Function. *Molecular Cell* **74**, 713-728.e6 (2019).
51. Dias, C. S., Araújo, N. A. M. & Telo da Gama, M. M. Dynamics of network fluids. *Advances in Colloid and Interface Science* **247**, 258–263 (2017).
52. Riback, J. A. *et al.* Viscoelasticity and advective flow of RNA underlies nucleolar form and function. *Molecular Cell* **83**, 3095-3107.e9 (2023).
53. Erdmann, P. S. *et al.* In situ cryo-electron tomography reveals gradient organization of ribosome biogenesis in intact nucleoli. *Nat Commun* **12**, 5364 (2021).
54. Ben-Shem, A. *et al.* The Structure of the Eukaryotic Ribosome at 3.0 Å Resolution. *Science* **334**, 1524–1529 (2011).

55. Kater, L. *et al.* Construction of the Central Protuberance and L1 Stalk during 60S Subunit Biogenesis. *Molecular Cell* **79**, 615-628.e5 (2020).
56. Wu, S. *et al.* Diverse roles of assembly factors revealed by structures of late nuclear pre-60S ribosomes. *Nature* **534**, 133–137 (2016).
57. Szaflarski, W. *et al.* Early rRNA processing is a stress-dependent regulatory event whose inhibition maintains nucleolar integrity. *Nucleic Acids Research* **50**, 1033–1051 (2022).
58. Berchtold, D., Battich, N. & Pelkmans, L. A Systems-Level Study Reveals Regulators of Membrane-less Organelles in Human Cells. *Molecular Cell* **72**, 1035-1049.e5 (2018).
59. Chhipi-Shrestha, J. K. *et al.* Splicing modulators elicit global translational repression by condensate-prone proteins translated from introns. *Cell Chemical Biology* **29**, 259-275.e10 (2022).
60. Ugolini, I. *et al.* Chromatin localization of nucleophosmin organizes ribosome biogenesis. *Mol Cell* **82**, 4443-4457.e9 (2022).
61. Sanders, D. W. *et al.* Competing Protein-RNA Interaction Networks Control Multiphase Intracellular Organization. *Cell* **181**, 306-324.e28 (2020).
62. Kwon, I. *et al.* Poly-dipeptides encoded by the C9orf72 repeats bind nucleoli, impede RNA biogenesis, and kill cells. *Science* **345**, 1139–1145 (2014).
63. Frottin, F. *et al.* The nucleolus functions as a phase-separated protein quality control compartment. *Science* **365**, 342–347 (2019).
64. Hiscox, J. A. RNA viruses: hijacking the dynamic nucleolus. *Nat Rev Microbiol* **5**, 119–127 (2007).
65. Shin, Y. & Brangwynne, C. P. Liquid phase condensation in cell physiology and disease. *Science* **357**, (2017).
66. McKinley, K. L. & Cheeseman, I. M. Large-Scale Analysis of CRISPR/Cas9 Cell-Cycle Knockouts Reveals the Diversity of p53-Dependent Responses to Cell-Cycle Defects. *Dev Cell* **40**, 405-420.e2 (2017).
67. Edelstein, A. D. *et al.* Advanced methods of microscope control using μManager software. *J Biol Methods* **1**, e10 (2014).
68. Pinkard, H. *et al.* Pycro-Manager: open-source software for customized and reproducible microscope control. *Nat Methods* **18**, 226–228 (2021).
69. van der Walt, S. *et al.* scikit-image: image processing in Python. *PeerJ* **2**, e453 (2014).
70. Wickham, H. *ggplot2: Elegant Graphics for Data Analysis*. (Springer-Verlag New York).
71. Tang Y, Horikoshi M, Li W. ggfortify: Unified Interface to Visualize Statistical Result of Popular R Packages. *The R Journal* **8**, 474--485 (2016).
72. Slowikowski, K. ggrepel: Automatically Position Non-Overlapping Text Labels with 'ggplot2'. (2023).
73. Kolde, R. pheatmap: Pretty Heatmaps. (2019).
74. Stirling, D. R. *et al.* CellProfiler 4: improvements in speed, utility and usability. *BMC Bioinformatics* **22**, 433 (2021).
75. Edgar, R. C. MUSCLE: multiple sequence alignment with high accuracy and high throughput. *Nucleic Acids Research* **32**, 1792–1797 (2004).
76. Stecher, G., Tamura, K. & Kumar, S. Molecular Evolutionary Genetics Analysis (MEGA) for macOS. *Mol Biol Evol* **37**, 1237–1239 (2020).